Petroleum Science 23 (2026) 1687–1711

Contents lists available at ScienceDirect

Petroleum Science

journal homepage: www.keaipublishing.com/en/journals/petroleum-science

Original Paper

Influencing factors and microscopic flow mechanism of shale oil during pressurized spontaneous imbibition in the Lucaogou Formation, Jimusar Sag: An experimental study

Xiao-Biao He [a,b], Qun Luo [a,b,*], Zhen-Xue Jiang [a,b], Qing-Qing Fan [a,b], Ying-Yan Li [c]

[a] *State Key Laboratory of Petroleum Resources and Engineering, China University of Petroleum (Beijing), Beijing, 102249, China*
[b] *Research Institute of Unconventional Petroleum Science and Technology, China University of Petroleum (Beijing), Beijing, 102249, China*
[c] *Research Institute of Exploration and Development, PetroChina Xinjiang Oilfield Company, Karamay, 834000, Xinjiang, China*

ARTICLE INFO

Article history:
Received 3 March 2025
Received in revised form
26 July 2025
Accepted 3 November 2025
Available online 8 November 2025

Edited by Xi Zhang and Jie Hao

Keywords:
Shale oil
Micro-oil distribution
Spontaneous imbibition
Connected pore
Multifractal theory
Wettability

ABSTRACT

Crude oil recovery and residual oil distribution at the microscopic pore scale are governed by pore structure, wettability, and imbibition dynamics. However, the evolution of pore structure and wettability during spontaneous imbibition and their impact on oil displacement efficiency remain poorly understood, particularly in saline lacustrine shale reservoirs with complex pore networks and variable wettability. The lack of a systematic framework linking imbibition to oil displacement efficiency hinders a comprehensive understanding of its controlling mechanisms, necessitating further investigation. Therefore, this study selected four typical lithologies from the Lucaogou Formation in the Jimusar Sag. Through a combination of methods, including high-pressure mercury intrusion (MIP), low-temperature N_2 adsorption (LTN$_2$A), CO_2 adsorption (CO_2GA), nuclear magnetic resonance (NMR), computer tomography scanning (CT), focused ion beam scanning electron microscopes (FIB–SEM) and QEMSCAN identification, along with multifractal theory and wettability index, the flow mechanisms of shale oil and the distribution of residual oil during pressurized spontaneous imbibition were investigated. The results: (1) All lithology samples exhibited a nonlinear recovery trend of “increase–decrease–increase” during pressurized spontaneous imbibition. (2) The pore connectivity of micritic dolomite is poor, with high heterogeneity. Dolomitic siltstone and arenaceous dolomite exhibit better mesopore connectivity and higher oil migration efficiency. Feldspathic lithic fine sandstone, with high pore connectivity, shows strong oil and gas aggregation and fluid transport capabilities in macropores. (3) Two typical residual oil distribution patterns and their controlling mechanisms were identified in the Lucaogou Formation shale reservoir: a macropore-dominated residual oil aggregation pattern associated with water-wet feldspathic lithic fine sandstones, and a micropore-mesopore dominated residual oil retention pattern commonly occurring in oil-wet micritic dolomite. This study systematically reveals the flow mechanisms of shale oil and the distribution of residual oil during pressurized spontaneous imbibition, based on the synergistic effects of mineral composition, pore structure, wettability, and capillary forces, providing a theoretical foundation and practical reference for improving shale oil recovery.

1. Introduction

In recent years, with the advancement of oil and gas exploration and development, shale oil, as a typical representative of unconventional oil and gas resources, has gradually become a focal point in global energy research (Zou et al., 2016; Pang et al., 2023; Gao et al., 2024). Shale oil is widely distributed in major oil and gas basins worldwide, with large-scale development achieved in formations such as the Bakken Shale in the Williston Basin, the Barnett Shale in the Fort Worth Basin, the Eagle Ford Shale in South Texas, and the fine-grained sedimentary rocks of the Shahejie Formation in the Dongying Sag of the Bohai Bay Basin, the Chang 7 Member of the Yanchang Formation in the Ordos Basin, the Longmaxi Formation in the Sichuan Basin, the Lucaogou Formation

---

* Corresponding author.
E-mail address: luoqun2002@net.com (Q. Luo).
Peer review under the responsibility of China University of Petroleum (Beijing).

https://doi.org/10.1016/j.petsci.2025.11.008

in the Junggar Basin, and the Qingshankou Formation in the Songliao Basin in China (French et al., 2020; Altawati et al., 2021; Xiao et al., 2024). Marine shale oil reservoirs in North America typically exhibit strong structural stability, regionally extensive cap and base layers, widespread high-quality source rocks, and high maturity, providing favorable geological conditions for efficient development (Guo et al., 2025). In contrast, due to complex geological and accumulation conditions, lacustrine shale oil reservoirs in China are characterized by high sensitivity, high water saturation, low porosity, and low permeability. Additionally, the fine pore-throat structures, poor connectivity, and strong reservoir heterogeneity further hinder effective fluid migration, resulting in significantly lower initial recovery rates compared to North American shale oil resources (Jin et al., 2021; Yuan et al., 2024). Furthermore, the high density, wax content, and low thermal maturity of lacustrine shale oil led to extremely poor fluidity. The diverse occurrence modes of shale oil further complicate its seepage mechanisms, making its flow behavior highly complex.

Spontaneous imbibition, as a key mechanism for wetting-phase fluids to displace non-wetting-phase fluids under external pressure or flow conditions, has garnered significant attention. Its driving forces include a combination of capillary pressure, viscous forces, and external pressure gradients, which significantly influence fluid flow in connected pores and ultimately affect recoverable reserves. (Cai et al., 2025; Xiao et al., 2025). Due to the presence of numerous nanoscale pore throats, shale reservoirs exhibit strong capillary effects, enabling wetting-phase fluids to efficiently displace non-wetting-phase fluids. Leveraging imbibition-driven oil recovery has become an effective strategy for enhancing shale oil recovery (Wijaya and Sheng, 2022). Research on shale imbibition has been extensively conducted worldwide, focusing mainly on the mechanisms, microscopic influencing factors, and key controls of imbibition-driven oil recovery (Wang et al., 2017; Afari et al., 2023). Studies have revealed that spontaneous imbibition characteristics are influenced by various parameters, including experimental conditions, fluid properties, mineral composition, and total organic carbon content. Among these, pore structure, sample geometry, fluid viscosity, initial water saturation, wettability, and interfacial tension are considered the core factors controlling the imbibition process. These factors collectively determine the dynamics and evolution of fluid distribution in shale reservoirs (Liu et al., 2023; Wang et al., 2024). However, quantitative studies on the mobilization of shale oil within nanoscale pores and the mechanisms for enhancing imbibition-driven oil recovery remain limited. The microscopic migration and displacement processes of wetting-phase fluids infiltrating the shale matrix via capillary action to displace non-wetting-phase fluids have not been fully elucidated. Currently, approximately 70% of crude oil remains trapped as residual oil in micropores and fractures, restricting efficient resource development (Lin et al., 2024). This phenomenon not only highlights the constraints imposed by the complex pore structure of shale reservoirs on the imbibition process but also underscores the significant potential for improving shale oil recovery.

The hydrocarbon content and occurrence state in reservoirs are critical for evaluating shale oil mobility and investigating seepage mechanisms, while pore structure and wettability are core factors controlling hydrocarbon enrichment and flow (Yang et al., 2025). The size distribution and connectivity of pores directly determine the seepage characteristics of reservoir fluids. Parameters such as pore size distribution, pore morphology, heterogeneity, and connectivity are fundamental to assessing shale reservoirs. These characteristics not only influence the efficiency of imbibition but also determine the reservoir's recovery potential (Zhang et al., 2022; Hu et al., 2024). Xia et al. (2021) highlighted that pore quantity, heterogeneity, and connectivity play crucial roles in imbibition efficiency. Reservoirs with poor connectivity often exhibit low recovery rates, whereas strong micropore connectivity significantly enhances imbibition efficiency. However, effective evaluation of pore connectivity and heterogeneity in shales remains a major challenge due to mixed wettability, complex mineral compositions, and other factors. Although studies employing CT and FIB–SEM technologies have characterized the multiscale, complex pore structures of shales, most focus on descriptive parameters like porosity and pore-throat size distribution (Zhu et al., 2021; Hosseini et al., 2021). For instance, 3D pore network models generated from CT scans visually assess pore connectivity, or connectivity is qualitatively evaluated using the proportion and coordination number of connected pores derived from pore network models. However, the directionality of pore throats and its relationship with pore connectivity, which is equally important for characterizing fluid flow, is often overlooked. Moreover, fractal dimensions demonstrate significant advantages in revealing pore structure heterogeneity. Previous studies have primarily used methods such as mercury intrusion, gas adsorption, and scanning electron microscopy to characterize rock pore complexity and analyze influencing factors through capillary constraint models and geometric models (Cui et al., 2022; Wang et al., 2025). However, optimizing fractal models and differentiating the complexity and influencing factors of pores with varying connectivity remain limited. Wettability, which reflects the tendency of fluids to spread or adhere on rock surfaces, directly affects the microscopic distribution of oil, gas, and water in reservoirs and the accumulation process (Elkhatib et al., 2024). Wettability is influenced by both mineral and organic compositions and is closely related to reservoir pore structure. The compositional complexity of shales results in diverse wettability behaviors, ranging from water-wet to neutral-wet or oil-wet (Xiao et al., 2025). Current research on shale wettability focuses on improvements in characterization methods, quantitative evaluations, and analysis of influencing factors. Techniques such as contact angle measurements, spontaneous imbibition, and NMR are commonly used to assess wettability, but their applications yield varied results (Sharifigaliuk et al., 2021). Most existing studies rely on static qualitative analyses, with limited research on quantitative evaluations and dynamic transition patterns of shale wettability under different occurrence states. In particular, the dynamic oil-rock interactions under the presence or intervention of aqueous phases remain relatively underexplored.

NMR technology plays a key role in reservoir pore structure and fluid analysis. Its relaxation signals are solely related to hydrogen atoms, and the T_2 spectrum accurately reflects pore characteristics and fluid distribution (Du et al., 2024a). Significant progress has been made in using NMR to characterize rock wettability and pore structure. Combined with gas adsorption and MIP, NMR can convert transverse T_2 into pore radius, enabling quantitative analysis of oil-water distribution across different pore size ranges (Fu et al., 2025). Furthermore, by calculating multifractal dimensions, the heterogeneity of pore distribution can be comprehensively revealed. Using heavy water to replace aqueous phases allows for the independent quantification of dynamic oil phase changes during imbibition, while real-time variations in the T_2 spectrum visually reflect the distribution and evolution of crude oil in pores of various scales (Wang et al., 2025). Based on NMR relaxation theory, an NMR wettability index calculation model can be established, providing an effective tool for further studying reservoir wettability and seepage characteristics (Al-Garadi et al., 2022).

The Junggar Basin, a significant superimposed hydrocarbon-bearing basin in northwest China, has witnessed remarkable progress in Permian shale oil exploration in recent years. The shale oil of the Lucaogou Formation in the Jimusar Sag has advanced to large-scale development, driving the establishment of a national shale oil demonstration zone. However, despite extensive research on the formation's depositional background, source rocks, reservoirs, source-reservoir associations, and enrichment characteristics, challenges remain (Zhang et al., 2024a; Cai et al., 2024; Li et al., 2024). The Lucaogou Formation, characterized by a saline lacustrine basin setting, high-frequency cyclic deposition, multi-source mixing, source-reservoir integration, thin-layer stacking, pervasive oil saturation, and localized enrichment, presents issues such as low recovery rates, rapid production decline, and short economic lifespans. Consequently, substantial volumes of crude oil remain trapped within reservoir pores and fractures (Wang et al., 2020). This study selected representative shale samples from the Lucaogou Formation and employed MIP, gas adsorption, NMR, magnetic resonance imaging (MRI), and CT experiments, combined with pressurized spontaneous imbibition tests. Utilizing multifractal dimensions and the NMR wettability index, the research distinguished fluid flow directions and identified connected pores to construct a visualized process of pressurized spontaneous imbibition across different shale lithologies. It elucidated the dynamic changes in oil-phase distribution during imbibition, investigated the mobilization characteristics of crude oil in pores of varying sizes, and quantitatively evaluated the recovery efficiency in micropores, mesopores, and macropores. Furthermore, it identified differences in shale oil mobility across lithologies, determined the residual oil distribution after pressurized spontaneous imbibition, and revealed the coupling relationship between pore structure and wettability on shale oil flowability. Finally, the study clarified the flow mechanisms of saline lacustrine shale oil under the influence of pressurized spontaneous imbibition.

2. Samples and methodologies

2.1. Samples

Shale samples were collected from the Permian Lucaogou Formation in the eastern Jimusar Sag, Junggar Basin (Fig. 1(a)). The Jimusar Sag covers an area of approximately 1500 km^2 and is a west-deep, east-shallow, west-faulted, east-overthrust graben structure (Fig. 1(b)). The Lucaogou Formation consists primarily of saline lacustrine-deltaic deposits (Zhang et al., 2024a). The lithology is influenced by saline water bodies, often containing carbonate mineral components such as quasi-synsedimentary dolomite and diagenetic calcite grains. This has led to the development of saline lacustrine mixed rock reservoirs, which is a distinctive characteristic of Lucaogou Formation shale oil, contrasting with the siliciclastic-carbonate mixed rocks typically found in marine environments (Luo et al., 2018; Zheng et al., 2019). The Lucaogou Formation is divided into two sections: the upper (P_2l_2) and lower (P_2l_1) units, each containing a “sweet spot” body that has been successfully developed for industrial oil flows (Sun et al., 2024). The “sweet spot” lithologies include arenaceous dolomite, feldspathic lithic fine sandstone, dolomitic siltstone, muddy siltstone, and micritic dolomite (Fig. 1(c)). Therefore, based on the typical lithologies of the upper and lower “sweet spot” bodies, four representative shale samples were selected for research: micritic dolomite, arenaceous dolomite, dolomitic siltstone, feldspathic lithic fine sandstone (Fig. 1(d)). The four lithological samples analyzed in this study were collected from Well J10060, covering the upper and lower “sweet spot” intervals of the Lucaogou Formation. Previous studies on these representative end-member lithologies in the Jimusar Sag have systematically characterized their mineral compositions and pore structures (Cao et al., 2024b; Zheng et al., 2019), providing a solid foundation for representativeness and comparison. The selected samples exhibit significant differences in mineral composition, pore structure, and reservoir properties, forming the basis for the comparative analysis in this study. Among them, the feldspathic lithic fine sandstone shows a porosity of 12.07% and a permeability of 0.771×10^{-6} μm^2, indicating good reservoir quality, whereas the micritic dolomite has a porosity of only 4.10% and a permeability of 0.018×10^{-6} μm^2, dominated by micropores and a dense structure, reflecting poor reservoir performance. All samples were drilled along fractures and cut into different specifications based on experimental requirements. The sample specifications for MIP, NMR, and pressurized spontaneous imbibition experiments were 25 mm × 25 mm; for CO_2GA and LTN$_2$A experiments, the samples were 60–80 mesh; for CT experiments, the samples were cubic blocks of 1 cm × 1 cm × 1 cm; and for QEMSCAN experiments, the sample size was 10 mm × 10 mm × 2 mm. The specific parameters for the samples used in pressurized spontaneous imbibition physical simulation experiments are listed in Table 1.

2.2. MIP, LTN$_2$A, and CO_2GA experiments

Due to the strong heterogeneity and lithological diversity of the Lucaogou Formation's lacustrine shale reservoirs, accurate pore size classification is critical for characterizing reservoir structure. At present, there is no unified standard for shale pore classification. Commonly used schemes include those proposed by Zhu el al. (2021), which categorize pores based on origin, size, and fluid interaction mechanisms. To enhance lithological comparability and align with international standards, this study adopts the International Union of Pure and Applied Chemistry (IUPAC) classification, which defines micropores (<2 nm), mesopores (2–50 nm), and macropores (>50 nm) based on pore diameter. This standard has been widely applied in pore structure studies of the Lucaogou Formation (Cao et al., 2024a, 2024b), demonstrating its regional applicability and reliability. Additionally, Given the continuum in scale and morphology between isolated pores and fractures, microfractures cannot be solely defined by a pore diameter >2 μm. Instead, identification incorporates geometric features observed in MAPs and QEMSCAN images, including linear extension, an aspect ratio >5, propagation lengths exceeding 10–20 μm, and characteristic orientations along bedding planes or across mineral grain boundaries (Guo et al., 2019; Yang et al., 2025). To systematically characterize pore structures, macropores were assessed using MIP, mesopores were analyzed using the LTN$_2$A method, and micropores were evaluated through CO_2GA. The AutoPore IV 9500 fully automated mercury porosimeter was employed to determine the pore size distribution from 3 nm to 1000 μm by measuring the volume of mercury intruded and extruded at varying pressures, in accordance with the national standard GB/T 21650.3-2011. The LTN$_2$A and CO_2GA experiments were conducted using the Micromeritics ASAP 2460 surface area and pore size analyzer, with the experiments adhering to industry standards GB/T 21650.3-2011 and GB/T 19587-2017, respectively. Prior to testing, the crushed samples were dried at 60 °C for 48 h to remove initial moisture from interconnected pore spaces, followed by degassing under high vacuum at 110 °C. LTN$_2$A was performed at 77 K, and CO_2GA was conducted at 273.15 K. The relative pressures for N_2 and CO_2 physical adsorption were 0.002–0.99 and 0.01 to 0.03, respectively, with the mesopore and micropore volumes

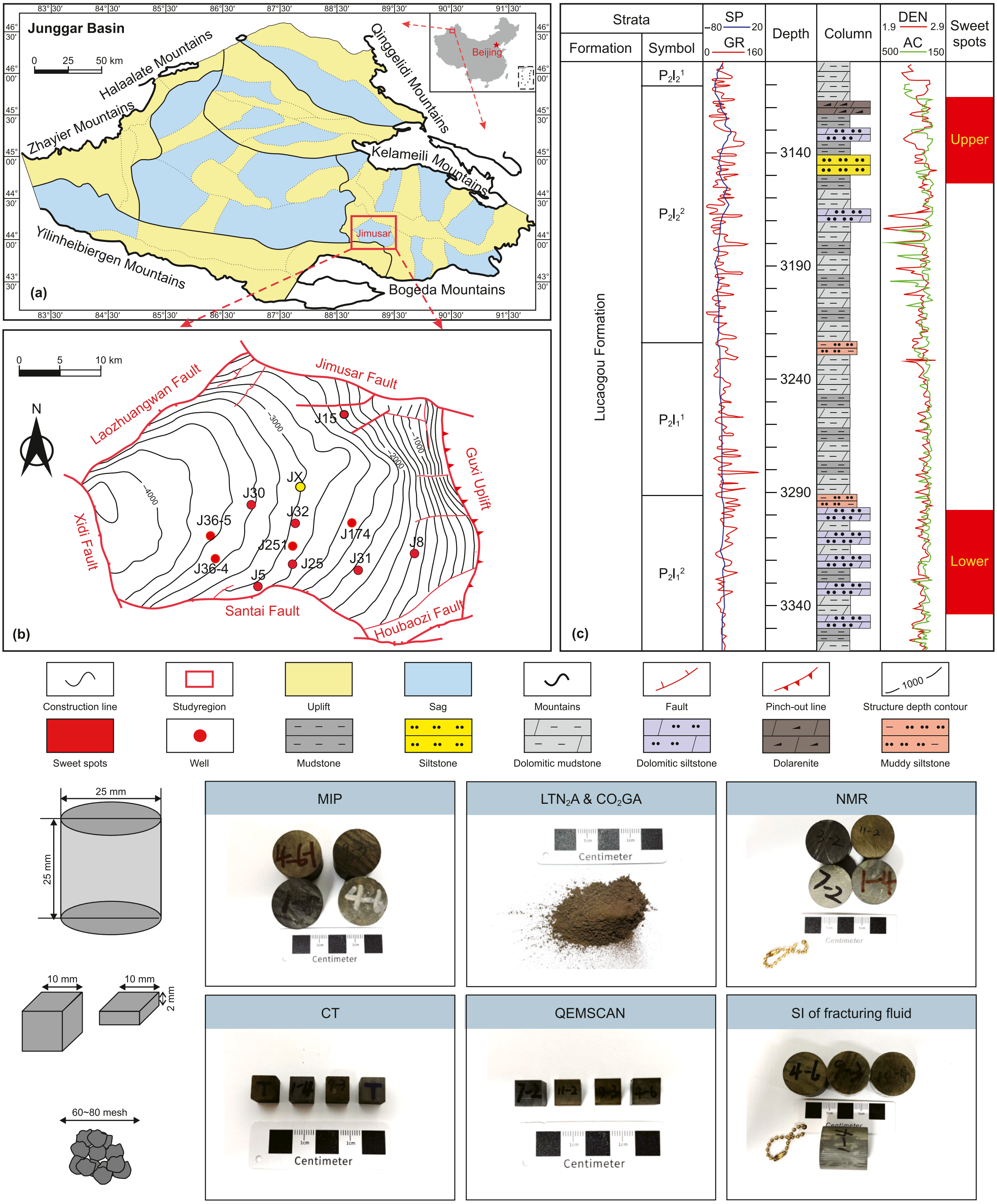

Fig. 1. Overview of the study area: (**a**) Structural unit map of the Junggar Basin; (**b**) top structure map of the Lucaogou Formation; (**c**) stratigraphic column of the Lucaogou Formation from Well J174 (modified from Zhang et al., 2024a); (**d**) photographs of experimental samples from Well J10060.

Table 1
Basic data of experimental core.

Sample	Well	Depth, m	Sweet spots	Lithology	Diameter, cm	Length, cm	Porosity, %	Permeability, 10^{-6} μm^2
10–4	J10060	4232.48	Upper	Feldspathic lithic fine sandstone	2.56	2.10	12.068	0.771
9–3	J10060	4227.84	Upper	Arenaceous dolomite	2.55	2.05	7.463	0.086
4–6	J10060	4240.16	Lower	Dolomitic siltstone	2.48	1.98	9.211	0.015
1–4	J10060	4242.00	Lower	Micritic dolomite	2.53	2.00	4.095	0.018

calculated using the Barrett-Joyner-Halenda and Dubin-Astakhov equations.

2.3. NMR and MRI

The NMR experiments were conducted at the State Key Laboratory of Petroleum Resources and Engineering, China University of Petroleum (Beijing), in strict accordance with the petroleum and natural gas industry standard SY/T6490-2014 “Laboratory Determination Methods for Rock Nuclear Magnetic Resonance Parameters.” The MesoMR23-060H-I core analyzer was employed, with a magnetic field strength of 0.52T and a resonance frequency of 21 MHz. To maintain the uniformity and stability of the magnetic field, the laboratory temperature was kept constant at 25 ± 0.5 °C, while the magnetic field temperature was controlled at 32 ± 0.1 °C. Given the small pore sizes in shale and the short relaxation times of water within the pores, the waiting time for measuring the NMR T_2 spectrum of shale samples was set to 3000 ms. To obtain more NMR responses from micropores, the echo spacing for all core NMR measurements was set to 0.07 ms, with 128 scans and 18,000 echoes collected.

A multi-layer spin-echo sequence was used to conduct MRI testing on shale samples, aimed at exploring the distribution characteristics of fluids within the rock. During the testing process, a linear gradient magnetic field was applied to the core samples, with layer selection encoding, frequency encoding, and phase encoding performed based on the differences in gradient field strength. Subsequently, mathematical inversion techniques were used to precisely spatially locate the NMR signals within the shale samples, generating vector MRI images perpendicular to the direction of fluid movement. This allowed for a direct visualization of the fluid distribution patterns and characteristics within the rock's pore system.

2.4. CT

The CT experiments were conducted at the State Key Laboratory of Petroleum Resources and Engineering, China University of Petroleum (Beijing), in strict compliance with the “Technical Specifications for Digital Core Processing and Analysis of Shale” (NB/T-11044-2022). The experiments utilized the Sanying nano Voxel 13502E CT scanner, which operates at a maximum power of 15 W, a maximum voltage of 90 kV, and a maximum resolution of 1.48 μm. Through detailed scanning and post-processing, high-resolution 3D pore structure models of shale samples were obtained, providing fundamental data for pore connectivity analysis.

2.5. FIB-SEM

The FIB-SEM experiment was conducted at the State Key Laboratory of Petroleum Resources and Engineering, China University of Petroleum (Beijing), following strict operational protocols. A FEI Helios NanoLab 650 FIB–SEM, comprising a dual beam system, was used, offering a maximum resolution of 0.8 nm. Shale samples were cut perpendicular to the bedding direction into thin slices (0.5 cm × 0.5 cm), mechanically polished, and then treated with argon ion beam polishing. Gold coating was applied to enhance conductivity, and the samples were mounted on the stage using conductive adhesive. Avizo 9.0 software was employed to unify voxel and display units to match scanning resolution, enabling 3D reconstruction and visualization of the shale microstructure.

2.6. QEMSCAN identification and MAPs imaging

QEMSCAN analysis was carried out at the State Key Laboratory of Petroleum Resources and Engineering, China University of Petroleum (Beijing), in strict accordance with the Rock and Mineral Analysis Technical Specification. Samples were prepared as 10 mm × 10 mm × 2 mm mounts, polished with an argon ion beam, coated with carbon, and placed in a scanning electron microscope. Target areas were selected for continuous backscattered electron imaging, and large-area mosaic images (MAPS) were generated through automated stitching to reveal the macroscopic distribution of reservoir space. QEMSCAN software was then used for in situ quantitative analysis of mineral composition, enabling precise identification of mineral distributions around pores in different lithologies.

2.7. Contact angle measurements

Contact angle measurements (CAM) were conducted using a JY-82C optical contact angle goniometer. Shale samples were first cut into 1 cm^3 cubes and polished to reduce surface roughness. The polished samples were then dried in a constant-temperature oven at 60 °C for 24 h. Deionized water was used as the testing fluid. Water contact angle measurements were performed on sample surfaces both parallel and perpendicular to the shale bedding.

2.8. Methodologies

2.8.1. NMR-PSD

The relaxation times in NMR testing consist of three components: surface relaxation time of rock particles, intrinsic relaxation time of the fluid, and molecular diffusion relaxation time.

$$\frac{1}{T_2}=\frac{1}{T_{2\mathrm{b}}}+\frac{1}{T_{2\mathrm{s}}}+\frac{1}{T_{2\mathrm{d}}} \tag{1}$$

where $T_{2\mathrm{b}}$ represents the NMR bulk relaxation time, an inherent property of the pore fluid, which is dependent on the fluid type; $T_{2\mathrm{s}}$ represents the surface relaxation time; and $T_{2\mathrm{d}}$ denotes the diffusion relaxation time. Since the bulk relaxation time is much longer than the surface relaxation time, and the inverse of diffusion relaxation time ($1/T_{2\mathrm{d}}$) approaches zero, the following relationship holds:

$$\frac{1}{T_2}=\frac{1}{T_{2s}}=\rho\frac{s}{v}=\rho\frac{F_s}{r} \tag{2}$$

where s represents the pore surface area, cm^2; v denotes the pore volume, cm^3; ρ is the surface transverse relaxation strength, μm/

ms; F_s is the pore shape factor, typically 2 for cylindrical pores and 3 for spherical pores; r is the pore radius, nm.

The NMR T_2 spectrum has a one-to-one correspondence with pore diameter (r) (Zhang et al., 2024b):

$$r = CT_2 \tag{3}$$

where C is a constant related to pore surface relaxation.

The determination of the conversion factor also requires error analysis. To select a conversion factor with minimal error, a function based on the error is used for selection:

$$\delta = \frac{\sqrt{\sum_2^n \omega_{(x_i)} \left(x_i - \omega_{x_i}\right)^2}}{\sqrt{\sum_2^n \omega_{(x_i)}}} \tag{4}$$

where δ represents the error; ω_{xi} indicates the pore diameter calculated using the currently selected conversion factor, μm; x_i is the pore diameter measured from CO_2GA, LTN_2A, and MIP data, μm; $\omega_{(xi)}$ represents the weighted percentage; and n denotes the number of test points in the pore diameter distribution.

2.8.2. Multifractal analysis

To reveal the heterogeneity of pore structures in shale reservoirs, this study calculates the multifractal dimensions of NMR data under various conditions using the box-counting method based on the T_2 spectra obtained from one-dimensional NMR experiments. Through normalized cumulative processing, the T_2 spectra are divided into N equal segments (ε), and the entire dataset undergoes interpolation. The probability mass function of the i-th segment can be expressed as (Gouyet and Bug, 1997):

$$P_i(\varepsilon) = \frac{N_i(\varepsilon)}{\sum_{i=1}^{N(\varepsilon)} N_i(\varepsilon)} \tag{5}$$

where $N_i(\varepsilon)$ represents the cumulative porosity or volume in the i-th partition; $P_i(\varepsilon)$ is the probability mass function.

According to multifractal theory, the probability mass function $P_i(\varepsilon)$ follows a power-law relationship with ε:

$$P_i(\varepsilon) \propto \varepsilon^{\alpha_i} \tag{6}$$

where α_i represents the Lipschitz-Hölder exponent or singularity strength, which characterizes the distribution density of the data. Lower α_i values indicate higher heterogeneity, while higher α_i values correspond to stronger regularity or uniformity.

For partition regions with the same singularity strength, the relationship between their frequency $N_\alpha(\varepsilon)$ and the partition scale (ε) can be defined as:

$$N_\alpha(\varepsilon) \propto \varepsilon^{-f(\alpha)} \tag{7}$$

where $f(\alpha)$ is the multifractal spectrum or singularity spectrum. An increase in the peak width of the spectrum indicates enhanced local heterogeneity, right-skewed spectra reflect sparse pore distribution, while left-skewed spectra correspond to regions of high aggregation probability.

The partition function is defined as:

$$X(q, \varepsilon) = \sum_{i=1}^{N(\varepsilon)} P_i(\varepsilon)^q \propto \varepsilon^{\tau(q)} \tag{8}$$

where q is the order moment or weight factor, ranging from $[-\infty, +\infty]$. When $q > 1$, it amplifies the information from high-aggregation regions; when $q < 1$, it emphasizes the information from low-aggregation regions. $\tau(q)$ is the mass function and can be expressed as:

$$\tau(q) = -\lim_{\varepsilon \to 0} \frac{\lg x(q, \varepsilon)}{\lg \varepsilon} = -\lim_{\varepsilon \to 0} \frac{\lg \sum_{i=1}^{N(\varepsilon)} P_i(\varepsilon)^q}{\lg \varepsilon} \tag{9}$$

where different q values correspond to different generalized fractal dimensions $D(q)$, which can be calculated using $\tau(q)$:

$$D(q) = \begin{cases} \dfrac{\tau(q)}{1-q} = \dfrac{1}{q-1} \dfrac{\lg \sum_{i=1}^{N(\varepsilon)} P_i(\varepsilon)^q}{\lg \varepsilon}, q \neq 1 \\[2ex] \dfrac{\sum_{i=1}^{N(\varepsilon)} P_i(\varepsilon) \lg P_i(\varepsilon)}{\lg \varepsilon}, q = 1 \end{cases} \tag{10}$$

The relationship between the singularity strength $\alpha(q)$, $f(\alpha)$, and $\tau(q)$ corresponding to the order moment q can be expressed as (Turcotte, 2002):

$$\alpha(q) = \frac{d\tau(q)}{dq} \tag{11}$$

$$f(\alpha) = q\alpha(q) - \tau(q) \tag{12}$$

where the generalized fractal spectrum q~$D(q)$ is used to extract the distribution characteristics of the dataset, and in the multifractal spectrum α~$f(\alpha)$, $\alpha(q)$, $f(\alpha)$, and the spectral width $\Delta\alpha$ are studied to investigate the distribution features of the dataset. The spectral width $\Delta\alpha$ is expressed as:

$$\Delta\alpha = \alpha_{\max} - \alpha_{\min} \tag{13}$$

The generalized fractal dimension spectrum $D(q)$ exhibits a characteristic inverted "S" curve, decreasing with the increase in order q. The greater the rate of decline, the stronger the sample's heterogeneity. When $q = -10$, $D(q)$ reaches its maximum value, $D_{\min}$, and when $q = 10$, $D(q)$ reaches its minimum value, $D_{\max}$. The overall width of the generalized fractal dimension spectrum, $\Delta D = D_{\min} - D_{\max}$, serves as a key indicator of the sample's overall heterogeneity, with larger values reflecting greater heterogeneity. Similarly, for the multifractal spectrum function $f(\alpha)$~α, the overall heterogeneity index is $\Delta\alpha = \alpha_{\max} - \alpha_{\min}$, where a larger value indicates stronger heterogeneity (Han et al., 2024).

2.8.3. Wettability index

When oil and water coexist within a rock, their respective relaxation times T_2 can be expressed as follows:

$$\frac{1}{T_{2,w}} = \frac{1}{T_{2b,w}} - \rho_{2,w} \frac{A_w}{V_w} \tag{14}$$

$$\frac{1}{T_{2,o}} = \frac{1}{T_{2b,o}} + \rho_{2,o} \frac{A_o}{V_o} \tag{15}$$

where $T_{2,w}$ and $T_{2,o}$ represent the relaxation times for water and oil, respectively, ms; $T_{2b,w}$ and $T_{2b,o}$ are the bulk relaxation times of water and oil, respectively, ms; $\rho_{2,w}$ and $\rho_{2,o}$ denote the surface relaxation rates of water and oil, respectively, μm/ms; A_w/V_w and A_o/V_o correspond to the surface-area-to-volume ratios of water and oil in the pores, μm^2.

To quantify shale wettability, Looyestijn and Jan Hofman (2006) proposed a wettability index I_w based on NMR technology, it is important to note that due to the diverse pore types and wide pore size distribution in shale reservoirs, pores of different sizes contribute differently to hydrocarbon flow and exhibit distinct wettability behaviors. Therefore, in this study, based on NMR–PSD, T_2 signal areas corresponding to different pore size intervals under oil-saturated and water-saturated conditions were extracted separately to calculate the wettability index (I_w) for each pore size range (Lin et al., 2024):

$$I_w = \frac{A_w - A_o}{A_w + A_o} \tag{16}$$

where A_w represents the total area of the T_2 signal under water-saturated conditions, μm^2; A_o represents the total area of the T_2 signal under oil-saturated conditions, μm^2; The wettability index I_w ranges from −1.0 to 1.0, where $I_w = -1.0$ denotes complete oil-wet conditions, $I_w = 0$ represents neutral wettability, and $I_w = 1.0$ indicates complete water-wet conditions.

Fleury et al. (2003) proposed a method to calculate the NMR wettability index using the peak relaxation times of rock cores under saturated water, saturated oil, bound water, and residual oil conditions. This method relies on T_2 spectral characteristics under extreme oil-water saturation, where the peak relaxation times of the dominant fluid are more reliable and minimally influenced by the secondary fluid. Additionally, Jia et al. (2024) derived a quantitative formula for the wettability index based on NMR relaxation theory and systematically investigated the dynamic evolution of rock wettability during water flooding using high-multiplicity sandstone core experiments. During water flooding, the effective separation of oil-water NMR signals, along with the significant differences between the T_2 spectrum of oil-saturated cores and the bulk relaxation time of oil, enables direct analysis of rock wettability changes based on oil-phase T_2 characteristics. Thus, using T_2 distributions measured at different spontaneous imbibition stages, the wettability index under varying oil saturations can be calculated (Jia et al., 2024):

$$I_w(R) = \frac{\dfrac{1}{T_{o,g}(S_{o1})} - \dfrac{1}{T_{bo,g}(S_{o1})} - 2S_o(R)\left[\dfrac{1}{T_{o,g}(R)} - \dfrac{1}{T_{bo,g}(R)}\right]}{\dfrac{1}{T_{o,g}(S_{o1})} - \dfrac{1}{T_{bo,g}(S_{o1})}} \tag{17}$$

where $I_{w(R)}$—NMR wettability index at different imbibition stages; $T_{o,g}(S_{o1})$—Geometric mean of the T_2 spectrum for oil in oil-saturated rock cores, ms; $T_{bo,g}(S_{o1})$—Geometric mean of the transverse bulk relaxation time for oil in oil-saturated rock cores, ms; $S_o(R)$—Oil saturation at different imbibition stages, %; $T_{o,g}(R)$—Geometric mean of the T_2 spectrum for oil at different imbibition stages, ms; $T_{bo,g}(R)$—Geometric mean of the transverse bulk relaxation time for oil at different imbibition stages, ms.

2.9. Experimental procedure

(1) The core samples were cleaned in an oil-removal apparatus using a dichloromethane-acetone mixture (3:1) at 90 °C and 0.3 MPa for 72 h to remove residual oil and soluble salts. To ensure the stability of core surface wettability and mineral chemistry during the experiments, reagents such as strong acids or bases that could disrupt the crystal lattice or alter surface functional groups were strictly avoided. The samples were then dried, weighed (recorded as the dry sample weight), and subjected to 1D-NMR and MRI scanning to obtain initial state parameters;

(2) After T_2 spectra were acquired for the dry samples, they were vacuum-saturated with 100% simulated oil. To minimize the influence of interfacial tension on wettability and more accurately simulate oil-water interfacial conditions in the reservoir, an imbibition agent was introduced during sample saturation with simulated oil. The agent consisted of hydrolyzed polyacrylamide (HPAM, molecular weight 7×10^6 g/mol), an alcohol ether nonionic surfactant (AEO-15), and hydrophilic nano-silica sol (NS), each at a concentration of 0.1 wt%. AEO-15 reduces oil-water interfacial tension to improve interfacial behavior; HPAM enhances viscosity matching and flow stability; and NS nanoparticles form a hydrophilic adsorption layer on pore surfaces, thereby strengthening water-wet characteristics (Yan et al., 2024). To eliminate free water signal interference during NMR testing, all agents were dissolved in D_2O. The samples were then reweighed and scanned again using 1D-NMR and MRI to characterize the oil-saturated state;

(3) Using tweezers, remove the saturated core, wipe off surface oil with gauze, and place the core into the pressure vessel of the "In-situ large-scale shale core oil-water imbibition and displacement simulation device" (Fig. 2). Submerge the core in heavy water, set the formation temperature to 75 °C and pressure to 27 MPa; place the core in the pressure vessel, adjust the temperature and pressure, and set five time intervals (6 h, 24 h, 48 h, 96 h, 144 h). After each interval, remove the core, weigh it, and perform 1D-NMR and MRI testing to observe the distribution of residual oil;

(4) Centrifuge the core, weigh it post-centrifugation, and perform T_2 spectrum and MRI tests.

3. Results

3.1. Image processing of MAPS and QEMSCAN

A comprehensive analysis of mineral composition and pore characteristics was conducted on four representative lithofacies of the Lucaogou Formation shale using MAPS, QEMSCAN, and FE–SEM. The results show that micritic dolomite is mainly composed of carbonate and clay minerals, characterized by predominantly fine, uniform intergranular and intragranular dissolution pores with small pore sizes, as well as linear microfractures with apertures of approximately 3–5 μm that propagate continuously along bedding planes and exhibit well-defined boundaries (Fig. 3(a)–(c)). Dolomitic siltstone is rich in quartz and dolomite, and develops abundant intergranular and dissolution pores (Fig. 3(d)–(f)). Arenaceous dolomite consists mainly of sand-sized lithic grains and dolomite, with low clay content and well-developed dolomite intercrystalline and dissolution pores, exhibiting a wide pore size range and complex pore morphology (Fig. 3(g)–(i)). Feldspathic lithic fine sandstone is primarily composed of feldspar, lithic fragments, and quartz, featuring coexisting intergranular and intragranular dissolution pores. Some microfractures propagate along the boundaries of quartz and feldspar grains, exhibiting curved morphologies with consistent orientation, together forming a complex pore-fracture network (Fig. 3(j)–(l)).

3.2. Full-scale pore-size distribution

Using the combined fitting method of CO_2GA, LTN_2A, and MIP for pore size distribution, alongside the cumulative pore volume and the inverse cumulative transverse relaxation time (T_2) spectra, the T_2 cutoff value was converted into specific pore sizes (Fig. 4). The results indicate that different lithological samples exhibit similar pore size peak distribution ranges, with mesopores and macropores accounting for the majority of the total pore volume, and macropores serving as the primary contributors to total pore volume (Fig. 4(a)–(d), (g), (j)). When the conversion coefficients ln(C) for micritic dolomite, dolomitic siltstone, arenaceous dolomite, feldspathic lithic fine sandstone were 4.01, 2.97, 3.32, and

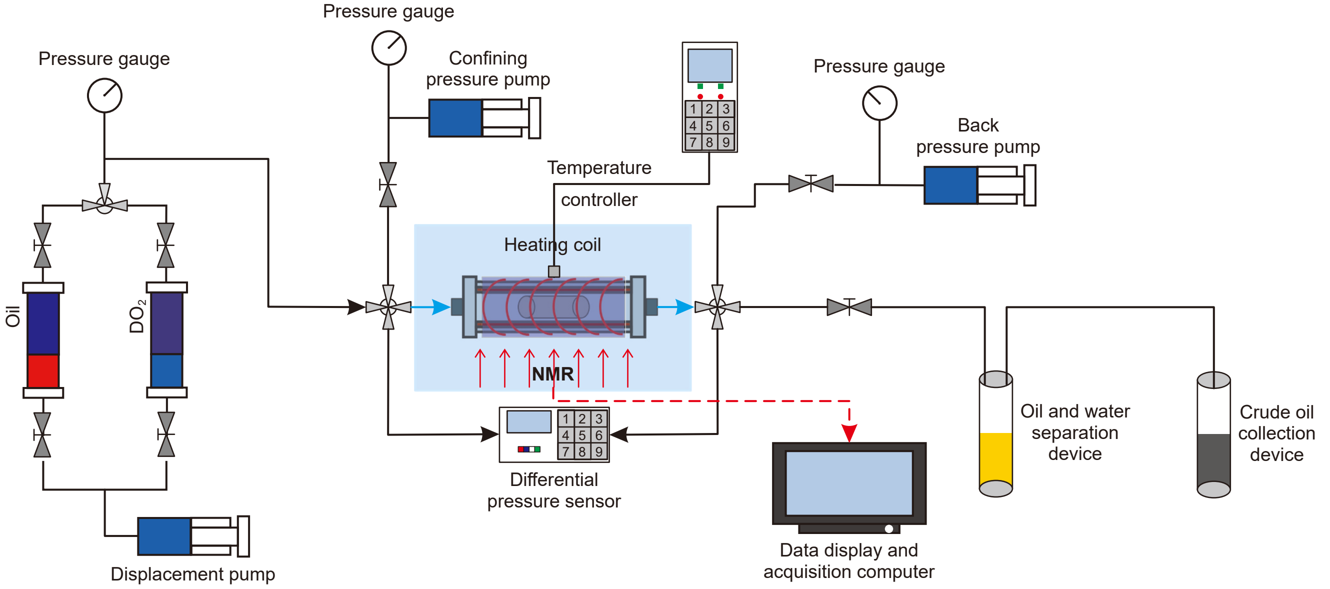

Fig. 2. Diagram of the pressurized spontaneous imbibition experimental setup for water-driven oil recovery based on NMR technology.

3.74, respectively (Fig. 4(b)–(e), (h), (k)), the shapes of the NMR T_2 spectra aligned well with the pore size distributions from CO_2GA, LTN_2A and MIP. Furthermore, after conversion, the peak positions of the T_2 spectra for all four core samples exhibited high consistency with the pore size distribution peaks obtained from the combined methods (Fig. 4(c)–(f), (i), (l)), demonstrating that the conversion coefficients derived from the error function are accurate and effectively reflect the relationship between transverse relaxation time and pore size (Hosseini et al., 2014).

3.3. *Quantitative analysis of multi-fractal characteristics in NMR T_2 spectra*

During the pressurized spontaneous imbibition process, the normalized cumulative T_2 spectra curves of micritic dolomite samples are positioned on the far left of the graph, with significant differences observed in the macropore stage across different imbibition stages, indicating poor connectivity and storage capacity, and the weakest pore structure (Fig. 5(a)). Conversely, the normalized curves of feldspathic lithic fine sandstone samples appear on the far right, with minimal differences between imbibition stages, reflecting superior connectivity and storage capacity and the most favorable pore structure (Fig. 5(j)). The normalized curves of dolomitic siltstone and arenaceous dolomite samples lie between these two extremes, showing moderate pore connectivity and structure (Fig. 5(d)–(g)). Shale samples of different lithologies exhibit distinct multifractal characteristics before and after imbibition. The generalized fractal dimension spectra $D(q)$ show that ΔD increases during the early stage of imbibition (6–48 h), indicating that larger pores are preferentially involved, thereby enhancing pore structure heterogeneity. As imbibition progresses, ΔD decreases, suggesting that smaller pores gradually participate, leading to a more homogeneous pore network (Fig. 5(b)–(e), (h), (k)). Correspondingly, the multifractal spectrum $f(\alpha)$ exhibits a rise-then-fall trend in both spectrum width $\Delta\alpha$ and $\alpha_{\max}$ (Fig. 5(c)–(f), (i), (l)), reflecting a transition in dominant pore size distribution from dispersed to concentrated and a temporal reduction in heterogeneity. These trends also imply dynamic changes in shale oil saturation across pore scales. The fluctuations in ΔD and $\Delta\alpha$ with time may be attributed to differences in pore structure and their lithology-dependent responses during the imbibition process.

3.4. *Pore network and quantitative analysis of connectivity*

Pore connectivity plays a critical role in hydrocarbon migration within shale reservoirs (Zheng et al., 2025). Based on 3D pore structure reconstruction models derived from micro-CT and FIB–SEM imaging, pore network models were generated using a centerline (skeletonization) algorithm to visualize multiscale connectivity across different lithologies. Isolated and connected pores were distinguished by color, and a pore-throat stick-ball model was constructed using the maximal ball algorithm, where spheres represent pores and cylinders represent throats. Throat orientation, which significantly influences fluid transport capacity in shale, was also quantified using the pore network model (Cui et al., 2022). Orientation was determined by measuring the angle between each throat and the *X*-axis in the XY plane (0°–360°), with 0°/180° aligned with the *X*-axis and 90°/270° with the *Y*-axis. Micro-CT results show that feldspathic lithic fine sandstone and dolomitic siltstone have significantly higher proportions of connected pores (15.20% and 10.72%, respectively) compared to arenaceous dolomite (6.45%) and micritic dolomite (5.63%) (Fig. 6(a)–(d), (g), (j)). Based on FIB–SEM analysis, although the overall proportion of connected pores decreases in feldspathic lithic fine sandstone and dolomitic siltstone (3.78% and 1.24%, respectively), both still exhibit a relative advantage. In contrast, the connectivity of arenaceous dolomite and micritic dolomite further declines to 1.60% and 0.96%, respectively (Fig. 7(a)–(d), (g), (j)). At the micrometer scale, the azimuthal orientation of pores in micritic dolomite exhibits a bimodal distribution, concentrated around 110° and 250°. Pores in dolomitic siltstone are predominantly aligned at 250°, showing a linear development. Arenaceous dolomite displays a bidirectional concentration at approximately 270° and 350°, while feldspathic lithic fine sandstone is characterized by a strong preferential orientation near 270° (Fig. 6(b)–(e), (h), (k)). At the nanometer scale, the azimuthal distributions vary slightly among lithologies: micritic dolomite shows a relatively dispersed distribution without a clear preferential direction; Arenaceous dolomite maintains a scattered pattern; Dolomitic

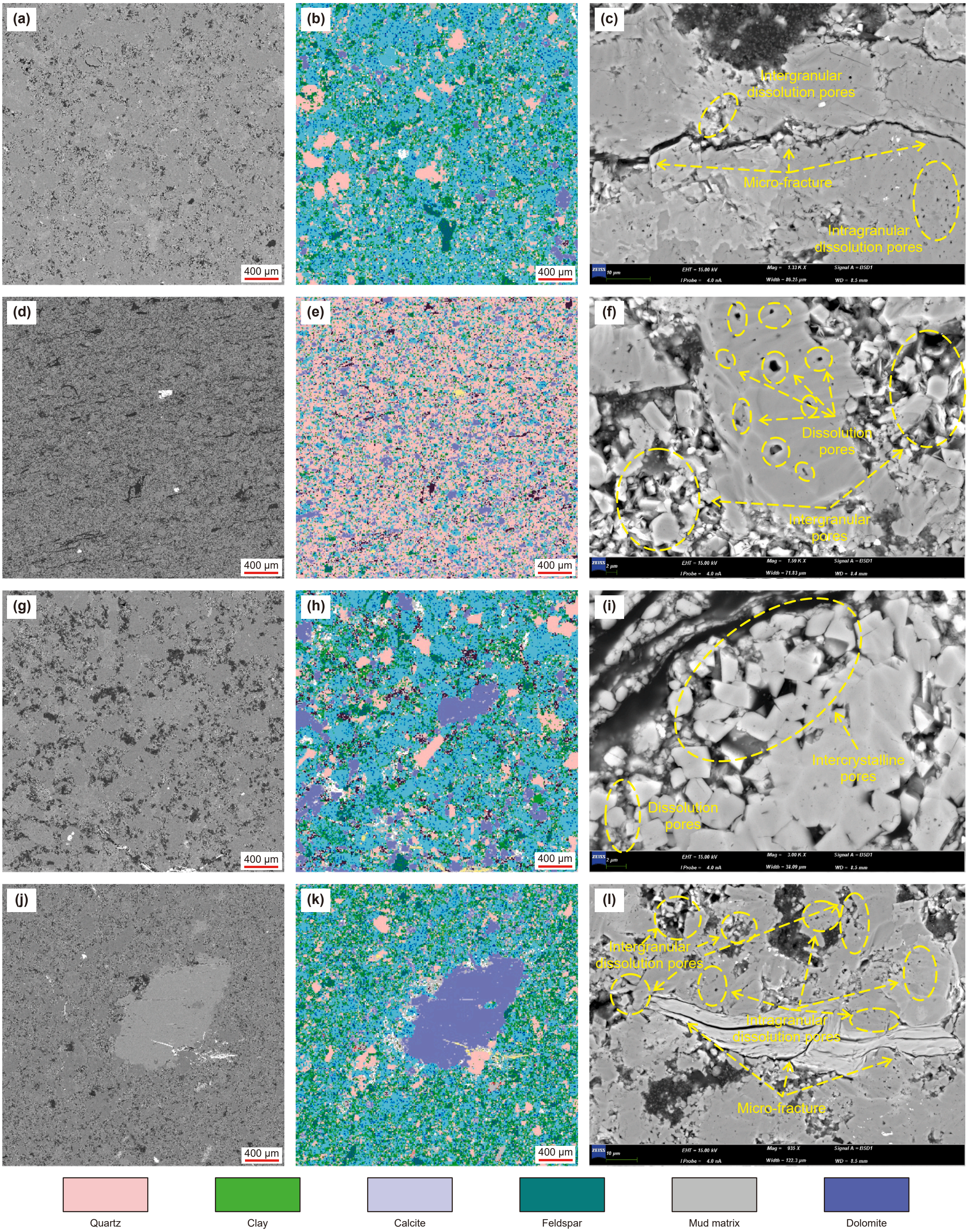

Fig. 3. The MAPS and QEMSCAN results effectively characterize the mineralogical and pore system features of these typical lithofacies in the Lucaogou Formation. (**a**)–(**c**) J10060 well, 4242 m, Micritic dolomite; (**d**)–(**f**) J10060 well, 4240.16 m, Dolomitic siltstone; (**g**)–(**i**) J10060 well, 4227.84 m, Arenaceous dolomite; (**j**)–(**l**) J10060 well, 4232.48 m, Feldspathic lithic fine sandstone.

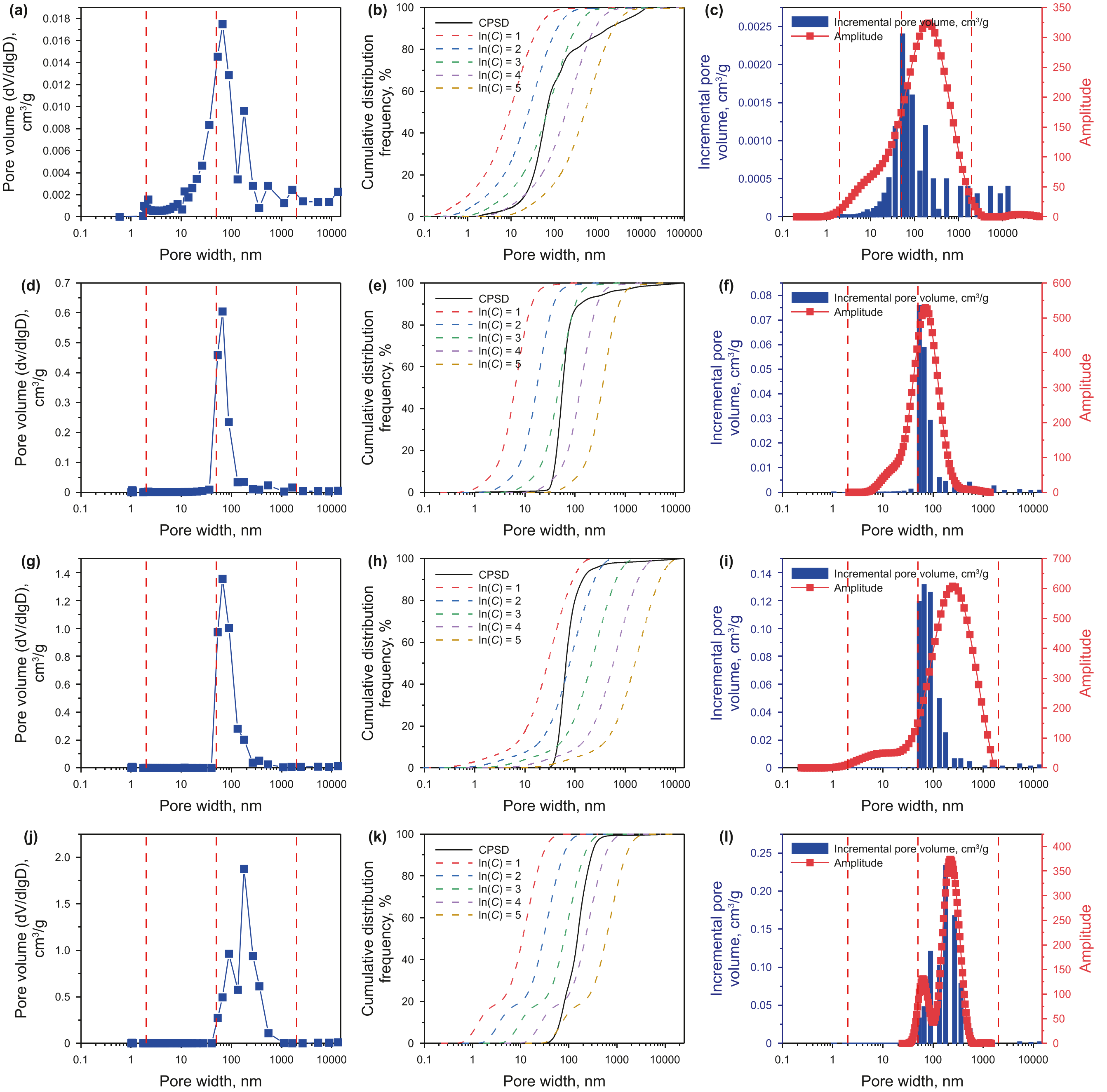

Fig. 4. Comparison of pore size distribution characteristics, NMR T_2 spectrum-to-pore size conversion relationships, and fitting results for different lithological samples. (**a**), (**b**), (**c**) Micritic dolomite; (**d**), (**e**), (**f**) dolomitic siltstone; (**g**), (**h**), (**i**) arenaceous dolomite; (**j**), (**k**), (**l**) feldspathic lithic fine sandstone. CPSD: combined pore size distribution.

siltstone exhibits a bimodal distribution; and feldspathic lithic siltstone shows enhanced concentration at 350° (Fig. 7(b)–(e), (h), (k)) (Table 2). These patterns suggest that throat orientation may influence reservoir fluid flow potential, though existing studies on its effect remain limited (Han et al., 2024). To further quantify connectivity, coordination number distributions for pores aligned with the *Z*-axis (coinciding with the spontaneous imbibition direction) were analyzed. At the microscale, average coordination numbers range from 1.34 to 1.86, with micritic and arenaceous dolomite concentrated at the lower end, while dolomitic siltstone and feldspathic lithic fine sandstone display higher and more balanced distributions, indicating superior 3D connectivity (Fig. 6(c)–(f), (i), (l)). At the nanoscale, coordination numbers decrease overall, but lithological differences remain consistent (Fig. 7(c)–(f), (i), (l)).

3.5. Shale wettability

Based on the T_2 distributions from imbibition experiments, wettability indices for different pore sizes under varying oil saturations were calculated. CAM using parallel- and cross-bedding water droplets were employed to assess the overall interfacial wettability along and across shale laminae, respectively. The results are as follows: Micropores in micritic dolomite exhibited stable oil-wet behavior throughout the experiment, with consistently negative wettability indices. Mesopores and macropores

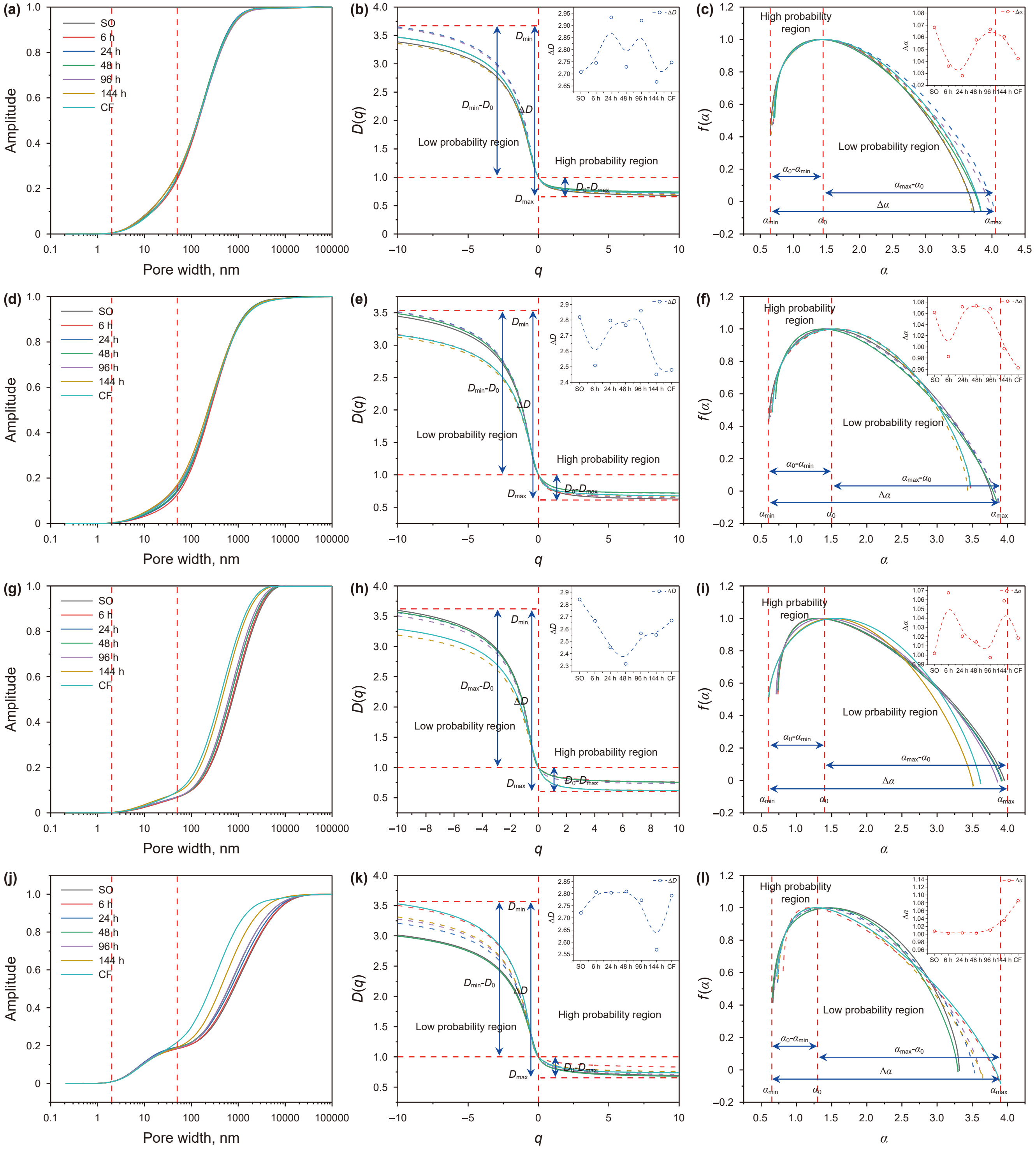

Fig. 5. Analysis of pore complexity in the Lucaogou Formation shale samples: (**a**), (**d**), (**g**), (**j**) normalized cumulative T_2 spectra; (**b**), (**c**), (**h**), (**k**) generalized fractal spectrum (q~$D(q)$); (**c**), (**f**), (**i**), (**l**) multifractal spectrum (α~$f(\alpha)$). (**a**), (**b**), (**c**) Micritic dolomite; (**d**), (**e**), (**f**) dolomitic siltstone; (**g**), (**h**), (**i**) arenaceous dolomite; (**j**), (**k**), (**l**) feldspathic lithic fine siltdstone.

showed water-wet characteristics, and their wettability indices increased over time. Contact angles for parallel- and cross-bedding water droplets were 85° and 72°, respectively, both indicating a predominantly water-wet surface (Fig. 8(a)). In dolomitic siltstone, micropores were initially water-wet but gradually approached neutral wettability over time. Mesopores shifted from water-wet to weakly water-wet, while macropores maintained strong water-wet behavior with increasing wettability indices. Contact angles along the bedding and across it were 50° and 76.5°, respectively, suggesting overall water-wet to neutral wettability (Fig. 8(b)). In arenaceous dolomite, micropores gradually transitioned from oil-wet to water-wet. Mesopores changed more rapidly, whereas macropores remained strongly oil-wet, with minimal changes in wettability indices. Contact angles reached

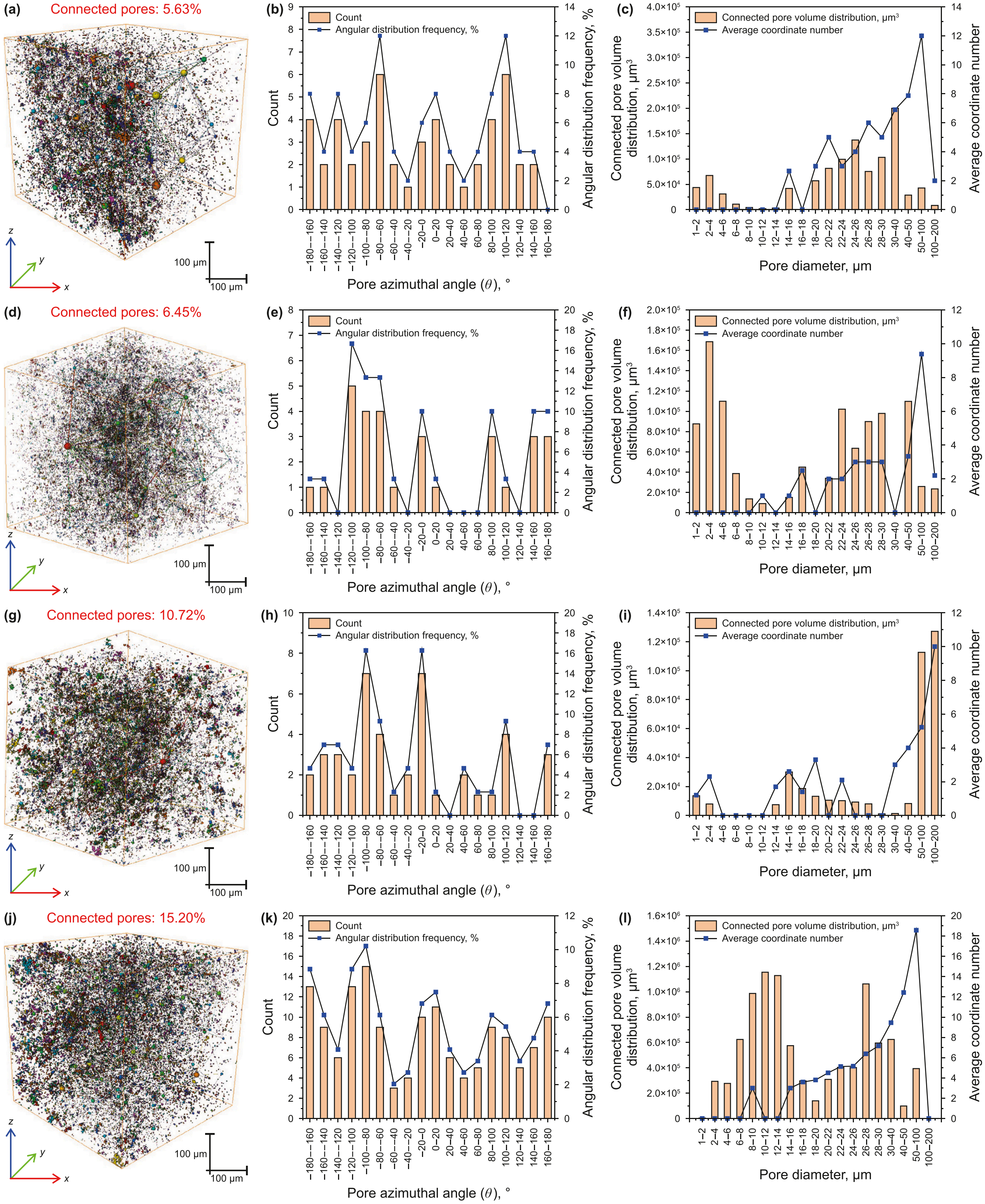

Fig. 6. Pore network model and quantitative analysis of pore connectivity of the sample from Micro-CT (resolution: 1.48 μm). (**a**), (**b**), (**c**) Micritic dolomite; (**d**), (**e**), (**f**) dolomitic siltstone; (**g**), (**h**), (**i**) arenaceous dolomite; (**j**), (**k**), (**l**) feldspathic lithic fine sandstone.

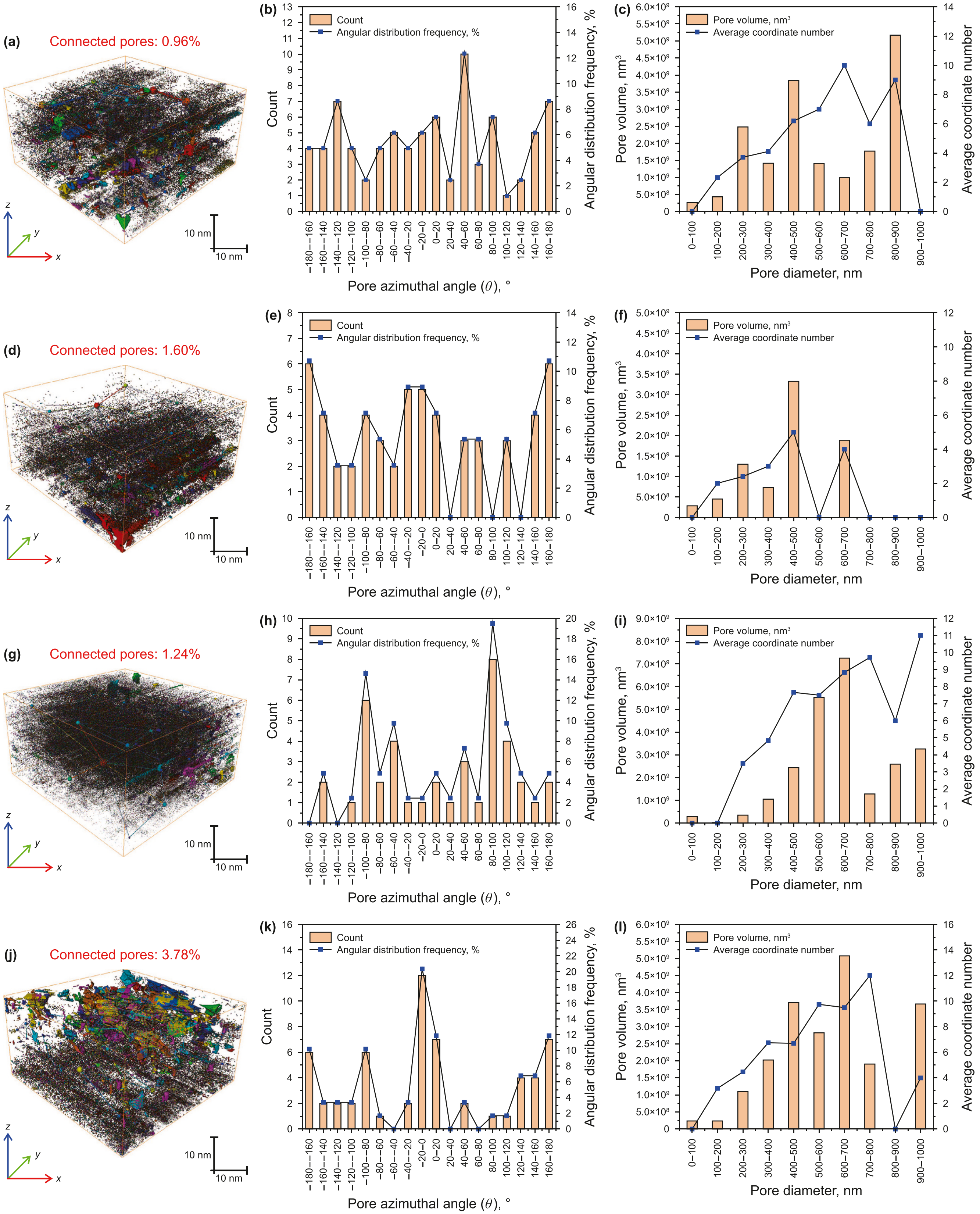

Fig. 7. Pore network model and quantitative analysis of pore connectivity of the sample from FIB–SEM (resolution: 20 nm). (**a**), (**b**), (**c**) Micritic dolomite; (**d**), (**e**), (**f**) dolomitic siltstone; (**g**), (**h**), (**i**) arenaceous dolomite; (**j**), (**k**), (**l**) feldspathic lithic fine sandstone.

Table 2
Multi-scale quantitative parameters of pore connectivity derived from Micro-CT and FIB-SEM.

Lithology	Connected pore volume, % (Micro-CT/FIB–SEM)	Average coordination number (Micro-CT/FIB–SEM)	Dominant throat orientation (Micro-CT/FIB–SEM)
Micritic dolomite	5.63/0.96	2.67-12.00/2.33-10.00	110°, 250°/50°, 170°, 230°
Dolomitic siltstone	10.72/1.24	1.00-9.38/2.00-5.00	250°/90°, 270°
Arenaceous dolomite	6.45/1.60	1.00-10.00/3.50-11.00	270°, 350°/170°
Feldspathic lithic fine sandstone	15.20/3.78	3.00-18.57/3.18-12.00	270°/350°

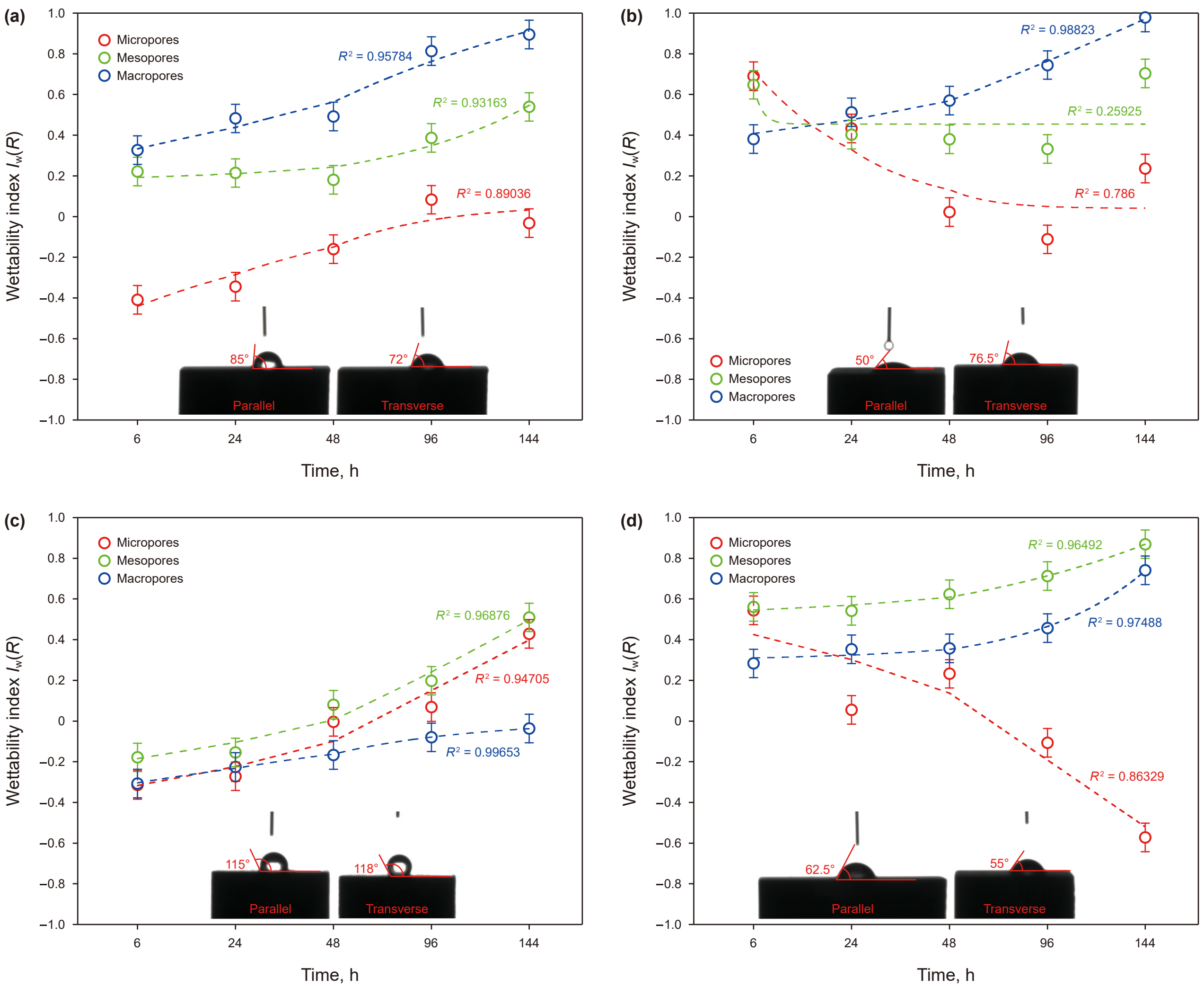

Fig. 8. Dynamic variations in wettability indices of micropores, mesopores, and macropores across different lithologies. (**a**) micritic dolomite; (**b**) dolomitic siltstone; (**c**) arenaceous dolomite; (**d**) feldspathic lithic fine sandstone. The error arises from baseline drift caused by the overlap of oil and water T_2 spectra signals (Looyestijn and Jan Hofman, 2006; Al-Garadi et al., 2022).

115° and 118° for the bedding-parallel and cross-bedding planes, respectively, indicating pronounced oil-wetness, consistent with the stable oil affinity of macropores (Fig. 8(c)). In feldspathic lithic fine sandstone, micropores, mesopores, and macropores initially exhibited weak water-wet behavior. Over time, micropores shifted to stable oil-wetness, while mesopores and macropores remained water-wet, with their wettability indices increasing significantly. Contact angles of 62.5° and 55° indicated water-wet surfaces, consistent with the hydrophilic behavior of meso- and macropores. The discrepancy between micropore wettability and overall contact angle results may be attributed to variations in organic matter distribution and mineral surface properties within the pores (Fig. 8(d)).

3.6. *Shale oil recovery within microscopic pores during pressurized spontaneous imbibition*

In order to evaluate the degree of shale oil recovery during pressurized spontaneous imbibition, the degree of simulated oil mobilization was calculated based on the area of NMR T_2 spectrum:

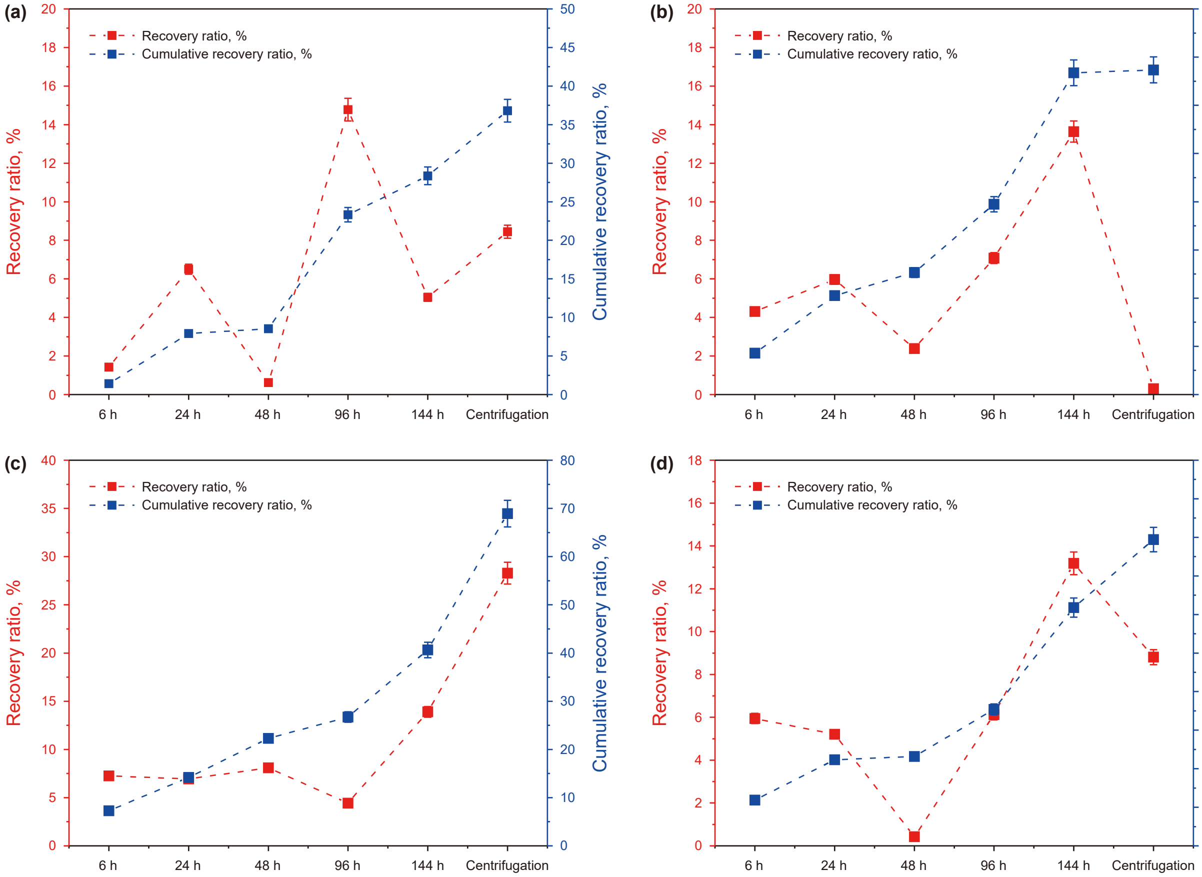

Fig. 9. Comparison of oil mobilization by pressurized spontaneous imbibition across different lithologies. (**a**) micritic dolomite; (**b**) dolomitic siltstone; (**c**) arenaceous dolomite; (**d**) feldspathic lithic fine sandstone. Recovery ratio (%): Oil recovery within a given time interval; Cumulative recovery ratio (%): Total oil recovered up to that time. The ±4% error in recovery factor is caused by the ambiguity of T_2 spectrum integration boundaries (Lin et al., 2024; Lv et al., 2025).

$$K = \frac{S_{\mathrm{os}} - S_i}{S_{\mathrm{os}}} \times 100\% \tag{18}$$

where K denotes the simulated oil recovery rate, %; S_{os}, the area of the core T_2 spectrum in saturated oil state, dimensionless; S_i, the area of the core T_2 spectrum under a certain action time, dimensionless.

Cumulative oil recovery from pressurized spontaneous imbibition simulations in different lithologies exhibits a continuous increase with imbibition time (Fig. 9). After 144 h, cumulative oil recovery in the four lithologies ranged from 28.36% to 40.63%. During pressurized spontaneous imbibition, all samples showed a non-linear “increase-decrease-increase” trend in recovery, reflecting complex interplay between pore structure, wettability, and fluid distribution (Lv et al., 2025). In the early stage (0–48 h), rapid recovery is attributed to the displacement of oil from larger pores and throats, where significant imbibition facilitates the expulsion of mobile fluids. During the intermediate stage (48–96 h), the recovery rate decelerates and may even temporarily decrease. This is due to the progressive depletion of easily accessible fluids, leading to more complex flow paths, particularly as oil becomes concentrated in micropores and irregular pores. Pore pressure equilibration further reduces imbibition efficiency. In the late stage (after 96 h), recovery increases again as prolonged imbibition gradually displaces residual oil from microfractures and nanopores. High capillary pressure in micropores drives the slow migration of residual oil. Finally, additional centrifugal displacement further enhances recovery by applying external pressure to expel residual oil, resulting in a secondary increase in recovery.

4. Discussion

4.1. Validity of calculation and characteristics of NMR-PSD

Based on the conversion coefficients derived in Section 3.2 using the error function, T_2 relaxation times were converted to pore diameters, and the NMR results were plotted alongside FIB-SEM data for comparison (Fig. 10). The results show that within the effective pore volume range captured by FIB–SEM, the trends of the NMR–PSD and FIB–SEM–derived pore size distribution (FIB–SEM–PSD) are generally consistent, confirming the reliability of the T_2-to-pore size transformation. However, FIB–SEM–PSD values are generally higher than those from NMR–PSD, which may be attributed to limitations in FIB–SEM's ability to characterize closed pores or complex pore networks (Zheng et al., 2019).

4.2. Characteristics of T_2 variation during pressurized spontaneous imbibition

NMR results indicate significant differences in pore structure and oil displacement characteristics among samples with varying lithologies during spontaneous imbibition. The pores in micritic dolomite are predominantly small, ranging from 10 to 1000 nm, with a notable reduction in macropores. The T_2 spectrum reveals that the peak amplitude of small pores is significantly higher than

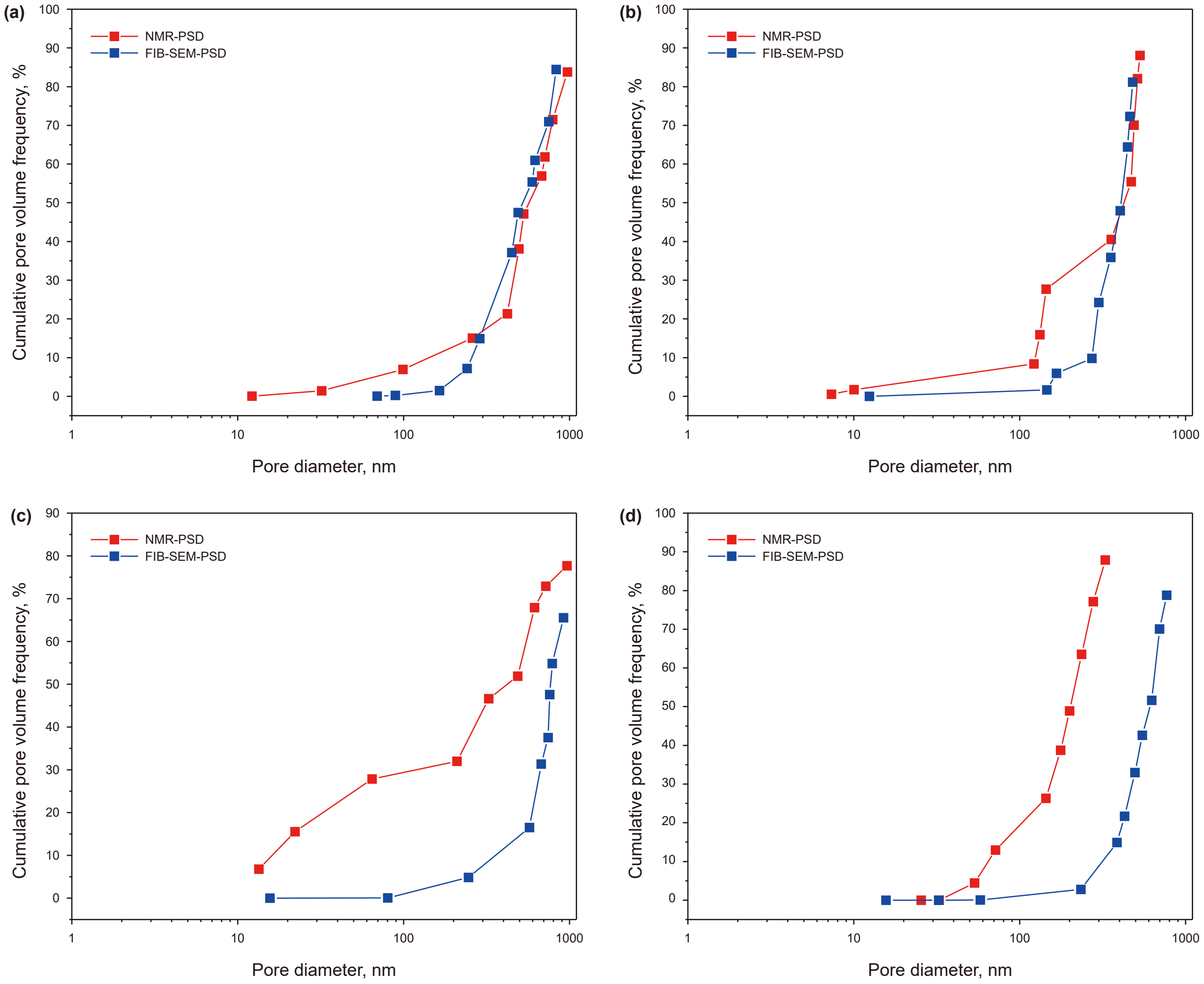

Fig. 10. Comparison of pore size distributions derived from NMR and FIB–SEM analyses.

that of other lithologies, indicating smaller pore sizes and poorer connectivity. During the initial imbibition stage, macropores contribute minimally, while the displacement process is dominated by a decline in signals from small pores, leading to low displacement efficiency. Even at 144 h and during the centrifugal stage, signals from small pores persist, highlighting the limited permeability of micritic dolomite and its significant restriction on the removal of residual oil (Fig. 11(a)). For dolomitic siltstone, pore distribution peaks are concentrated in the range of 100–1000 nm, with pore sizes larger than those in micritic dolomite. In the early imbibition stage (6 h), oil in macropores is rapidly displaced, resulting in a sharp decline in T_2 signals. After 24 h, small pores gradually contribute to the displacement process, although at a slower pace. During the centrifugal stage, some oil remains trapped in small pores, indicating their binding effect on residual oil (Fig. 11(b)). The pore distribution in arenaceous dolomite exhibits a wider range, from micropores smaller than 10 nm to macropores exceeding 1000 nm, with a distinct bimodal distribution. Small pores have a higher proportion and signal amplitude than those in other lithologies. In the early stage of imbibition (6 h), T_2 signals from macropores decline rapidly, while signals from small pores decrease more slowly. After 144 h, the proportion of residual oil in small pores remains high, suggesting limited contributions to oil production due to high wettability, which constrains displacement efficiency (Fig. 11(c)). In feldspathic lithic fine sandstone, pore sizes are primarily distributed between 100 and 10,000 nm, also showing a bimodal pattern. During the initial 6 h of imbibition, a rapid decline in T_2 signals from macropores indicates their dominance in early oil displacement, whereas the slower decline in signals from small pores reflects delayed displacement. After 144 h, signals from small pores stabilize, with residual oil predominantly retained in nanopores. This retention, influenced by nanopore effects and wettability, makes further displacement challenging (Fig. 11(d)).

To quantify the utilization degree of pores within different pore size ranges during the displacement process, we adopted the pore oil saturation formula (Utilization degree of different pores), defined as (Du et al., 2024b):

$$P_{\mathrm{oci}} = \frac{\sum_{T_{2,\min}}^{T_{2,\max}} A_{i,j} - \sum_{T_{2,\min}}^{T_{2,\max}} A_{i,0}}{\sum_{T_{2,\min}}^{T_{2,\max}} A_{i,b}} \times 100\% \tag{19}$$

where $T_{2,\min}$ and $T_{2,\max}$ are the minimum and maximum T_2 relaxation times from NMR measurements, respectively, ms; $A_{\mathrm{i,j}}$ is the T_2 signal intensity under oil-saturated conditions; $A_{\mathrm{i,0}}$ represents the signal intensity under different experimental states; $A_{\mathrm{i,b}}$ denotes the baseline signal intensity of the NMR instrument, A/m.

The calculated results reveal the dynamic changes in oil saturation within micropores, mesopores, and macropores over

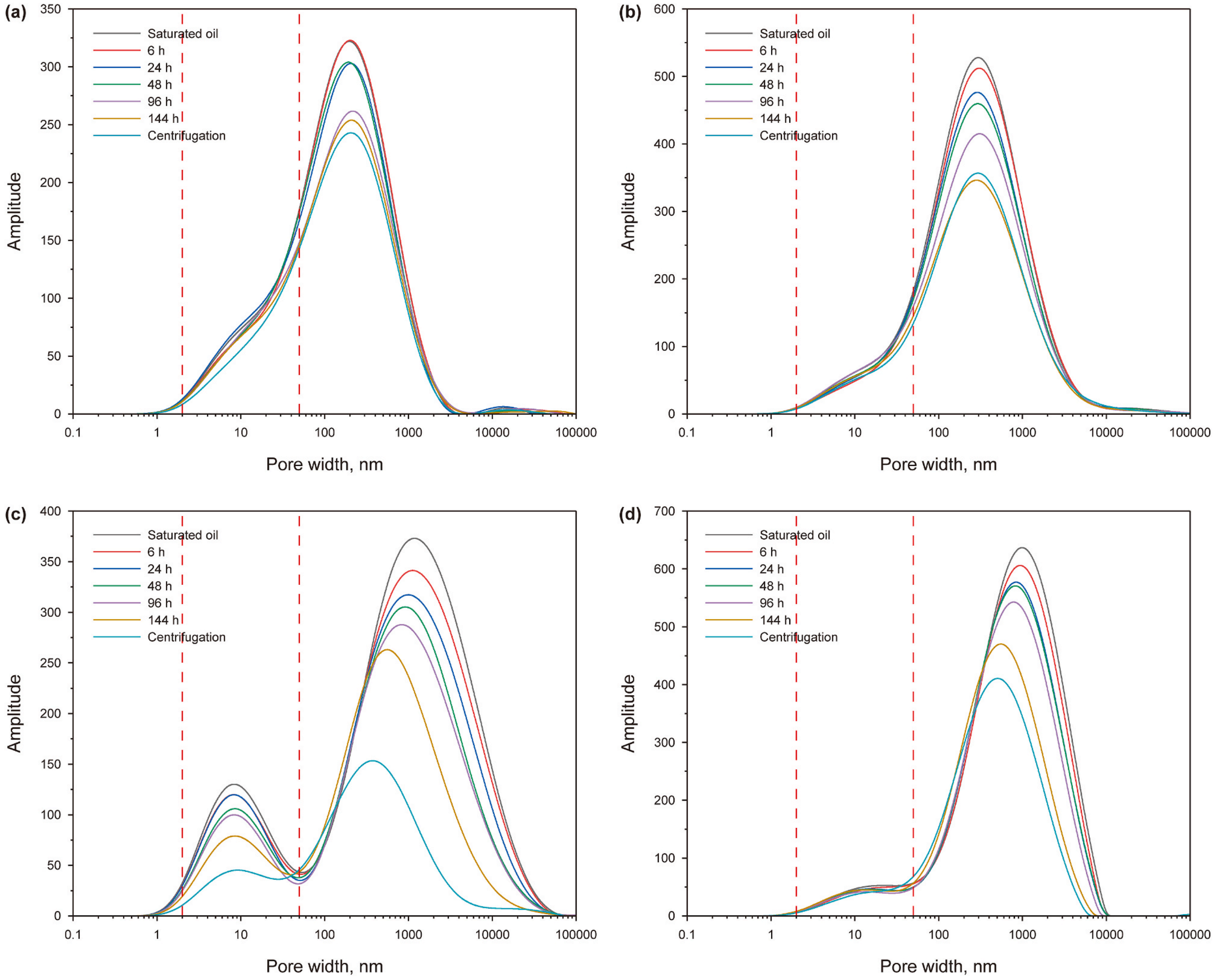

Fig. 11. NMR T_2 of core pressurized spontaneous imbibition for oil displacement. (**a**) micritic dolomite; (**b**) dolomitic siltstone; (**c**) arenaceous dolomite; (**d**) feldspathic lithic fine sandstone.

displacement time for different lithologies. The overall trend indicates a gradual decline in oil saturation with displacement time, but significant variations are observed across pore size scales in different lithologies. For micritic dolomite, oil saturation exhibits distinct staged variations (Fig. 12(a)). In micropores, oil saturation shows complex nonlinear changes: a slight increase during the initial displacement phase (6 h), a rapid decline within 24 h, and a subsequent increase during the later stages (96–144 h). The initial increase may be driven by capillary forces causing oil migration from macropores to micropores, while the subsequent decline results from water invasion into micropores. The later increase likely reflects residual oil redistribution, where capillary forces trap oil within micropores, demonstrating their strong retention effect on residual oil. In contrast, oil saturation in mesopores and macropores decreases steadily over time, with macropores exhibiting a faster decline. This indicates that macropores serve as primary pathways for water invasion, significantly enhancing displacement efficiency. The lower displacement efficiency in mesopores may be attributed to poor pore connectivity and higher capillary resistance. For dolomitic siltstone, oil saturation displays notable fluctuations over time (Fig. 12(b)). In micropores and mesopores, oil saturation slightly increases during 24–48 h, indicating oil redistribution during displacement, potentially caused by capillary forces driving oil migration to well-connected micropores and mesopores. Meanwhile, oil saturation in macropores declines rapidly to near zero, suggesting that macropores are the main pathways for water invasion during displacement. Their favorable wettability and connectivity significantly enhance water displacement efficiency. For arenaceous dolomite, oil saturation declines uniformly with displacement time across all pore size scales (Fig. 12(c)), resulting in a low residual oil saturation (approximately 15%). This indicates a low oil retention capacity for sandy dolomite, likely due to its uniformly distributed medium-to-large pore structures and good connectivity, which facilitate effective water penetration and oil displacement. Additionally, the high displacement efficiency may correlate with its wettability characteristics, further promoting oil desorption and migration. In feldspar lithic fine sandstone, oil saturation decreases consistently across micropores, mesopores, and macropores during displacement. Oil saturation in macropores drops rapidly to near zero during the initial stage, indicating that macropores are the primary pathways for water invasion. Their excellent connectivity and low capillary resistance enable rapid water displacement of oil, demonstrating high displacement efficiency (Fig. 12(d)). The decline rate of oil saturation in mesopores is intermediate between that of macropores and micropores, reflecting the moderate

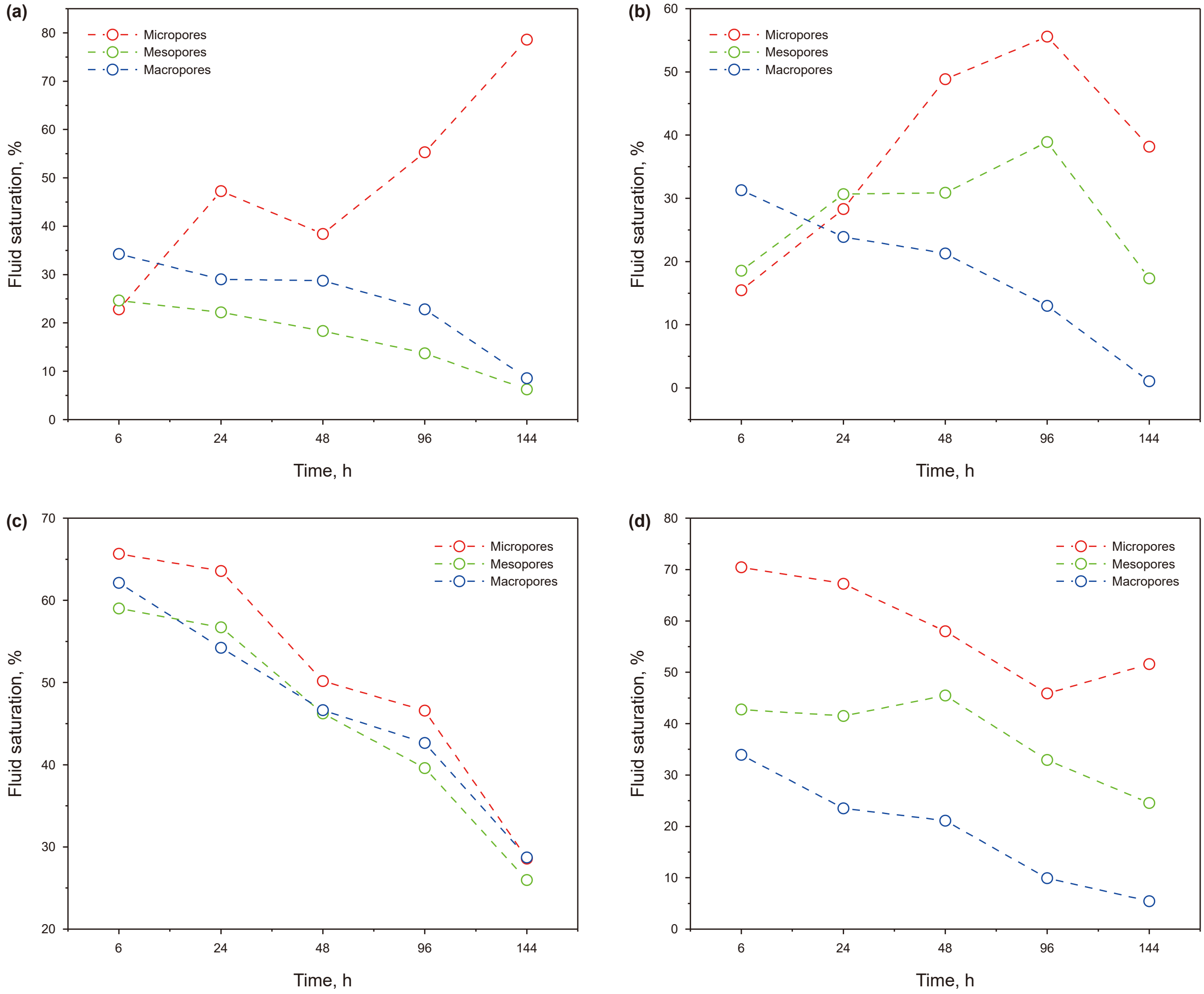

Fig. 12. Characteristics of fluid saturation changes in shale at different pressurized spontaneous imbibition stages. (**a**) Micritic dolomite; (**b**) dolomitic siltstone; (**c**) arenaceous dolomite; (**d**) feldspathic lithic fine sandstone.

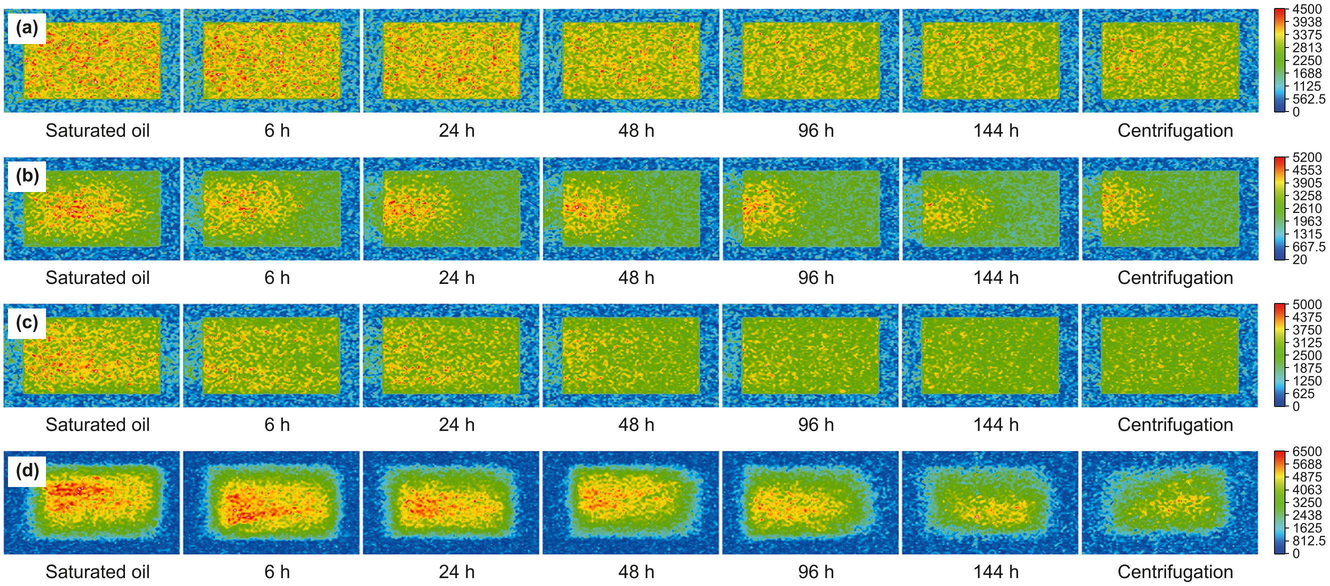

Fig. 13. MRI images of residual oil content changes during the pressurized spontaneous imbibition process of different lithologies. (**a**) Micritic dolomite; (**b**) dolomitic siltstone; (**c**) arenaceous dolomite; (**d**) feldspathic lithic fine sandstone.

restriction of capillary resistance on displacement efficiency. Micropores exhibit a slow decline in oil saturation throughout the process, with a significantly lower reduction compared to mesopores and macropores, indicating a strong retention capacity for residual oil. This phenomenon may result from high capillary resistance and low connectivity in micropores, hindering complete water invasion. Additionally, the presence of oleophilic surfaces within micropores may promote oil retention during the later displacement stages.

4.3. MRI-based residual oil evolution during pressurized spontaneous imbibition

Based on MRI imaging technology, the residual oil saturation evolution during the pressurized spontaneous imbibition and centrifugal displacement processes was quantitatively analyzed by monitoring the residual oil distribution at different time points and centrifugal stages for four typical lithologies of the Lucaogou Formation. The experimental results indicate that pore connectivity, heterogeneity, and pore size distribution are the critical factors affecting fluid flow efficiency (Fig. 13).

The initial MRI signal distribution of micritic dolomite was sparse, with negligible saturation decline after displacement and substantial residual oil retention after centrifugation (Fig. 13(a)), reflecting its extremely tight pore structure and lack of effective connectivity, which almost halted fluid flow. For dolomitic siltstone, the MRI images revealed a strongly heterogeneous oil saturation distribution, with high-saturation zones concentrated in the sample's center and edge saturation below 20%. After displacement, residual oil was mainly trapped in isolated pores or dead ends, and significant residual oil persisted after centrifugation, indicating that its pore structure is constrained by high heterogeneity (Fig. 13(b)).

The oil saturation of arenaceous dolomite was relatively low before displacement, concentrated in the 35%–50% range. Saturation reduction during displacement was limited, declining only to around 20% after 144 h, with noticeable residual oil remaining in isolated regions along pore edges after centrifugation. This suggests limited connectivity and weak inter-pore flow capacity (Fig. 13(c)). In contrast, the MRI images of feldspathic lithic fine sandstone displayed high and uniform oil saturation, with signals concentrated in high-saturation zones above 50%. Oil saturation rapidly decreased to below 10% within 6–144 h of displacement, achieving displacement efficiencies over 90%, with minimal residual oil remaining after centrifugation. This demonstrates superior pore-throat size and connectivity, significantly enhancing oil recovery efficiency (Fig. 13(d)).

4.4. Influencing factors of pressurized spontaneous imbibition

Reservoir pore characteristics are critical in determining fluid storage and migration behaviors, significantly influencing shale oil recovery (Cai et al., 2024). By integrating multi-parameter analyses, this study systematically explores the effects of pore volume, connectivity, heterogeneity, wettability, and the displacement efficiency of different lithological pores on shale oil recovery, revealing the relative contributions of various pore types to reservoir development (Fig. 14).

Pore volume plays a significant role in determining the cumulative oil recovery of shale reservoirs (Lin et al., 2024). Among the various pore types, mesopores and microfractures exhibit strong positive correlations with cumulative recovery ($R^2 = 0.82973$ and $R^2 = 0.65720$, respectively), whereas macropores and micropores show weaker correlations ($R^2 = 0.32642$ and $R^2 = 0.02753$) (Fig. 14(a)). Micropores, while contributing to hydrocarbon adsorption and storage, have limited impact on fluid migration due to their extremely small diameters and high flow resistance. Macropores, though offering larger storage space, are constrained by poor continuity and low fluid saturation, thus playing a limited role in imbibition. In contrast, mesopores provide a favorable balance between storage capacity and connectivity, facilitating both fluid retention and migration. Microfractures serve as critical flow pathways that enhance the overall connectivity of the pore system. This has also been supported by previous studies, for example, Li et al. (2024) demonstrated that microfractures reduce oil–mineral surface adhesion, thereby improving imbibition efficiency; Lin et al. (2024) further reported that microfractures restructure the pore network and accelerate fluid transport, effectively enhancing shale oil recovery.

The correlation between pore connectivity and cumulative shale oil recovery varies significantly across different scales (Fig. 14(b)). Connectivity derived from Micro-CT exhibits a strong linear relationship with recovery efficiency ($R^2 = 0.97577$), indicating that micron-scale connected pores play a dominant role in enhancing spontaneous imbibition. The correlation between nanopore connectivity characterized by FIB–SEM and oil recovery is extremely weak ($R^2 = 0.05418$), which may be attributed to two factors. First, although nanopores account for a large proportion of the reservoir, their extremely small pore sizes and narrow throats restrict fluid pathways, limiting their contribution to macroscopic displacement processes. Second, threshold settings during image processing significantly affect the identification accuracy of pores <50 nm, often leading to omission or misinterpretation of connected pathways and thus a systematic underestimation of connectivity (Cui et al., 2022). Moreover, NMR studies have shown that under capillary pressure dominance, even nanopore systems with low geometric connectivity can sustain effective spontaneous imbibition, contributing substantially to oil recovery (Al-Garadi et al., 2022). Notably, when connectivity data from both scales are integrated, the correlation remains high ($R^2 = 0.95468$), further confirming the synergistic role of multiscale connected pore networks in controlling imbibition efficiency.

The influence of pore heterogeneity on oil recovery was investigated. Oil recovery increased progressively with imbibition time and exhibited notable variations across different ranges of ΔD and $\Delta\alpha$, reflecting the complexity of fluid flow within distinct fractal regions (Fig. 14(c) and (d)). In the early stage (6–48 h), recovery was low and mainly associated with low ΔD and $\Delta\alpha$ values, indicating that fluid preferentially occupied larger, well-connected pores. As imbibition progressed (48–96 h), the fluid began to access more complex pore structures, with expanded ΔD and $\Delta\alpha$ ranges and a marked increase in recovery. Notably, in regions with high ΔD, the recovery improvement was more pronounced, suggesting that highly heterogeneous pore networks enhance fluid mobility. Notably, ΔD and Δα exhibit a significant negative correlation with pore connectivity (Fig. 14(e)). Elevated ΔD and Δα values indicate strong pore size heterogeneity, often associated with the development of numerous isolated micro- and nanopores, which reduce coordination numbers and hinder effective connectivity. This trend aligns with previous findings: poorer connectivity corresponds to more complex pore networks, broader multifractal spectra, and increased heterogeneity and flow resistance (Fan et al., 2022; Sun et al., 2024).However, during the later stage (96–144 h), although ΔD and $\Delta\alpha$ continued to expand, the recovery rate plateaued, indicating that most accessible pores had been occupied and displacement efficiency declined. Thus, while ΔD and $\Delta\alpha$ have limited direct correlation with recovery as standalone metrics, the structural complexity and heterogeneity they represent fundamentally control fluid displacement efficiency (Gao et al., 2024). Mineral composition is a key factor

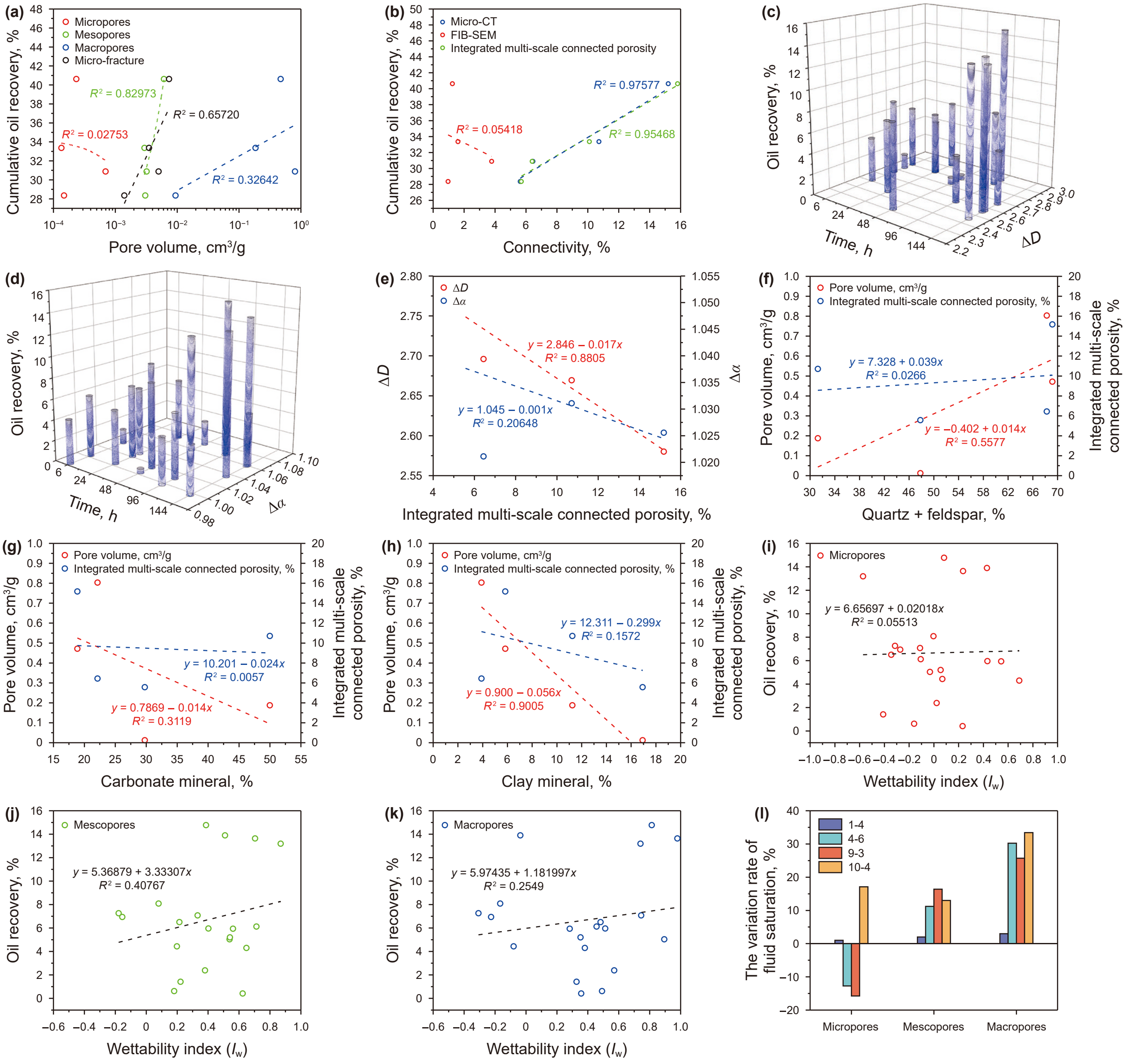

Fig. 14. Influencing factors of pressurized spontaneous imbibition.

influencing shale pore volume and connectivity. Quartz + feldspar content shows a moderate positive correlation with pore volume ($R^2 = 0.5577$), indicating that rigid mineral frameworks help preserve pore structure during compaction and enhance reservoir space (Fig. 14(f)). In contrast, clay mineral content exhibits a strong negative correlation with pore volume ($R^2 = 0.9005$), as the ductile, compact, and easily deformable nature of clays leads to collapse and compaction of associated pores, thereby reducing effective reservoir capacity (Fig. 14(g)). Carbonate minerals also show a negative correlation with pore volume ($R^2 = 0.3119$), possibly due to the influence of carbonate dissolution on pore development (Fig. 14(h)). Trends in pore connectivity closely mirror those in pore volume, suggesting that mineral composition not only controls pore size but also directly affects the development of flow pathways.

Pore wettability significantly influences fluid distribution and migration within the reservoir (Cai et al., 2024). The weak correlation between micropore wettability index and recovery ($R^2 = 0.05513$) suggests that micropore wettability has limited impact on fluid displacement (Fig. 14(i)). This is mainly attributed to the extremely small size of micropores, where fluids predominantly exist in adsorbed or capillary-bound states with negligible permeability, thus contributing little to macroscopic flow. In contrast, the mesopore wettability index exhibits a moderate positive correlation with recovery ($R^2 = 0.40767$), indicating that weak water-wet or mixed-wet conditions enhance oil and gas migration in mesopores (Fig. 14(j)). Under such conditions, the water phase may form continuous pathways along the pore walls, facilitating oil movement toward macropores or fractures. Moreover, mixed-wettability allows for dual-phase flow, with water displacing oil in some pores and oil films maintaining flow in others. The correlation between macropore wettability index and recovery is lower ($R^2 = 0.2549$), but the trend suggests that weak oil-wet or mixed-wet conditions may promote fluid displacement in macropores. Under weak oil-wet conditions, the oil phase tends to form continuous films along pore walls, confining water to the pore center or bypass channels, thereby reducing blockage. A wettability pattern of oil-wet macropores and water-wet micropores may create continuous oil pathways and reduce residual oil saturation (Fig. 14(k)). Significant differences in micropore, mesopore, and macropore displacement efficiencies were observed across lithological samples (Fig. 14(l)). Feldspathic lithic fine sandstone demonstrated the highest micropore displacement efficiency, reflecting superior pore connectivity. In contrast, micritic dolomite exhibited nearly zero micropore displacement efficiency, while arenaceous dolomite and dolomitic siltstone showed negative micropore displacement efficiencies. This anomaly could be related to strong capillary forces between micropores and mesopores, causing fluid migration into new fractures rather than effective mesopore displacement (Yan et al., 2024). Arenaceous dolomite, dolomitic siltstone, and feldspathic lithic fine sandstone exhibited higher mesopore displacement efficiencies, all approaching 20%, indicating that mesopores provided well-connected pathways for fluid migration. Limited by lower pore connectivity, micritic dolomite showed poor mesopore displacement performance. Arenaceous dolomite, dolomitic siltstone, and feldspathic lithic fine sandstone demonstrated high macropore displacement efficiencies, underscoring the critical role of macropores in fluid storage and migration. However, micritic dolomite exhibited low macropore displacement efficiency, possibly due to strong fluid retention effects.

4.5. Flow mechanism of Lucaogou Formation shale oil during pressurized spontaneous imbibition

Based on the multi-dimensional relationship between oil-water distribution in shale reservoirs under different lithology types, mineral composition, pore structure, wettability, and capillary forces, a differential flow model for saline lacustrine shale oil reservoirs was constructed. This model systematically reveals the oil-water distribution and displacement mechanisms during pressurized spontaneous imbibition in shale reservoirs, driven by the synergistic effects of mineral composition, pore structure, wettability, and capillary forces (Fig. 15). Variations in mineral composition among different lithofacies samples directly influence pore structure and wettability characteristics, thereby significantly affecting pressurized spontaneous imbibition behavior and the distribution of residual oil. In shale reservoirs, the pronounced differences in mineralogy govern pore architecture and wettability, which in turn control fluid distribution and displacement efficiency. The Lucaogou Formation was deposited in a hypersaline, reducing lacustrine environment and retained reductive conditions during subsequent diagenesis. This depositional-diagenetic setting exerted strong control over the development of mixed sedimentary systems, resulting in distinct lithofacies assemblages between the upper and lower “sweet spot” intervals. Such vertical lithological variations further intensified heterogeneity in pore structure, wettability, and imbibition behavior, ultimately exerting a direct influence on fluid migration mechanisms and the spatial distribution of residual oil (Fig. 15(a)).

Micritic dolomite, dominated by carbonate minerals, exhibits low pore volume and poor connectivity, with distinctly oil-wet characteristics. In contrast, feldspathic lithic fine sandstone is rich in quartz and feldspar, resulting in higher pore volume and better connectivity, and displays water-wet behavior. Arenaceous dolomite and dolomitic siltstone, with more diverse mineral compositions, show intermediate wettability characteristics between the two endmembers (Fig. 15(b)).

In shale oil reservoirs, organic matter is inherently oil-wet, while the wettability of inorganic minerals is primarily governed by their surface charge under geological conditions. As crude oil molecules are generally negatively charged, minerals with positively charged surfaces tend to be oil-wet, whereas those with negative charges exhibit water-wet behavior. For example, quartz and feldspar exhibit negative surface charges under weakly alkaline to neutral conditions, while carbonate minerals show positive charges in alkaline environments. The Lucaogou Formation was deposited in a weakly alkaline, saline lacustrine setting under arid climatic conditions. Consequently, the dominant water-wet minerals in the reservoir include quartz, albite, orthoclase, and clays, while carbonate minerals and organic matter are primarily oil-wet components (Chen et al., 2025). In water-wet systems, hydrophilic mineral surfaces are covered with water films, allowing capillary forces to drive oil toward larger pores. In oil-wet systems, oil is more readily retained in smaller pores. In mixed-wet systems, mineral surface heterogeneity leads to localized wettability contrasts, restricting effective oil migration (Fig. 15(c)) (Cao et al., 2023; Tangparitkul et al., 2023).

Capillary-driven spontaneous imbibition is a key mechanism for fluid transport in shale, governed by the combined effects of capillary pressure, viscous forces, gravity, and inertia. The pore characteristics and wettability of different lithologies dictate the capillary force regime, thereby controlling the distribution pattern of residual oil (Fig. 15(d)) (Tian et al., 2021; Kong et al., 2024). In the Lucaogou Formation shale reservoir, residual oil predominantly exhibits two distinct distribution patterns: a macropore aggregation model governed by water-wet conditions and a micro-mesopore retention model dominated by oil-wet behavior. These patterns are jointly controlled by mineral composition, pore structure, wettability, and capillary forces. The macropore aggregation mode commonly develops in lithologies rich in siliceous minerals, such as feldspathic lithic fine sandstone with high pore connectivity. Hydrophilic minerals like quartz and feldspar enhance the capillary adsorption capacity of the water phase, allowing it to preferentially enter narrower pores and displace oil into larger ones, resulting in the accumulation of oil droplets within macropores. This pattern is associated with high displacement efficiency, where oil exists mainly as isolated droplets or clusters in medium-to-large pores, indicating favorable connectivity and recovery potential. In contrast, the micro-mesopore retention mode typically forms in carbonate-rich lithologies such as micritic dolomite and some dolomitic siltstones. The strong oil-wet nature promotes oil adhesion to pore surfaces, forming film-like structures. Capillary resistance in micro- and mesopores significantly inhibits water invasion, causing oil to remain as films or dispersed droplets in fine pores. Under this model, displacement efficiency in micropores is nearly negligible, and mesopores also exhibit low efficiency, with residual oil present as adsorbed films or disconnected droplets, resulting in overall poor recovery.

It should be noted that under in-situ high-temperature and high-pressure conditions, pore structure evolution and wettability alterations significantly influence shale oil imbibition and recovery. On one hand, elevated geostress compresses nanopores and narrows pore throats, reducing connectivity and suppressing imbibition rates (Chen et al., 2025; Emmings et al., 2020). On the other hand, high-pressure conditions enhance the hydrophilicity of clay minerals, potentially weakening capillary-driven imbibition efficiency. However, microfracture opening can create new oil-wet pathways that partially offset the compaction effect. Previous studies have shown that under high-temperature and high-

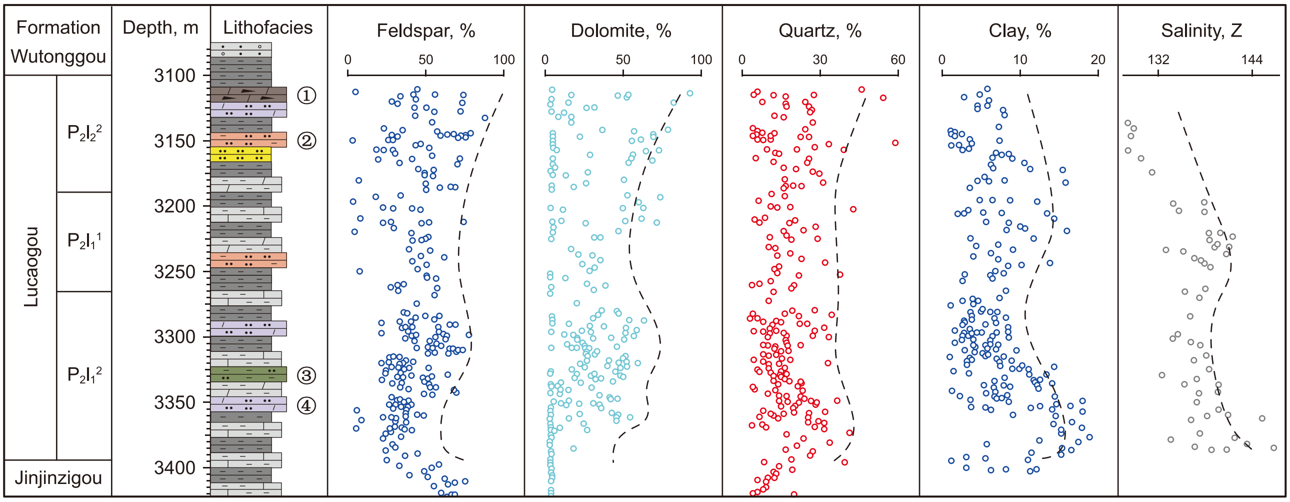

(a) Differences in mineral composition

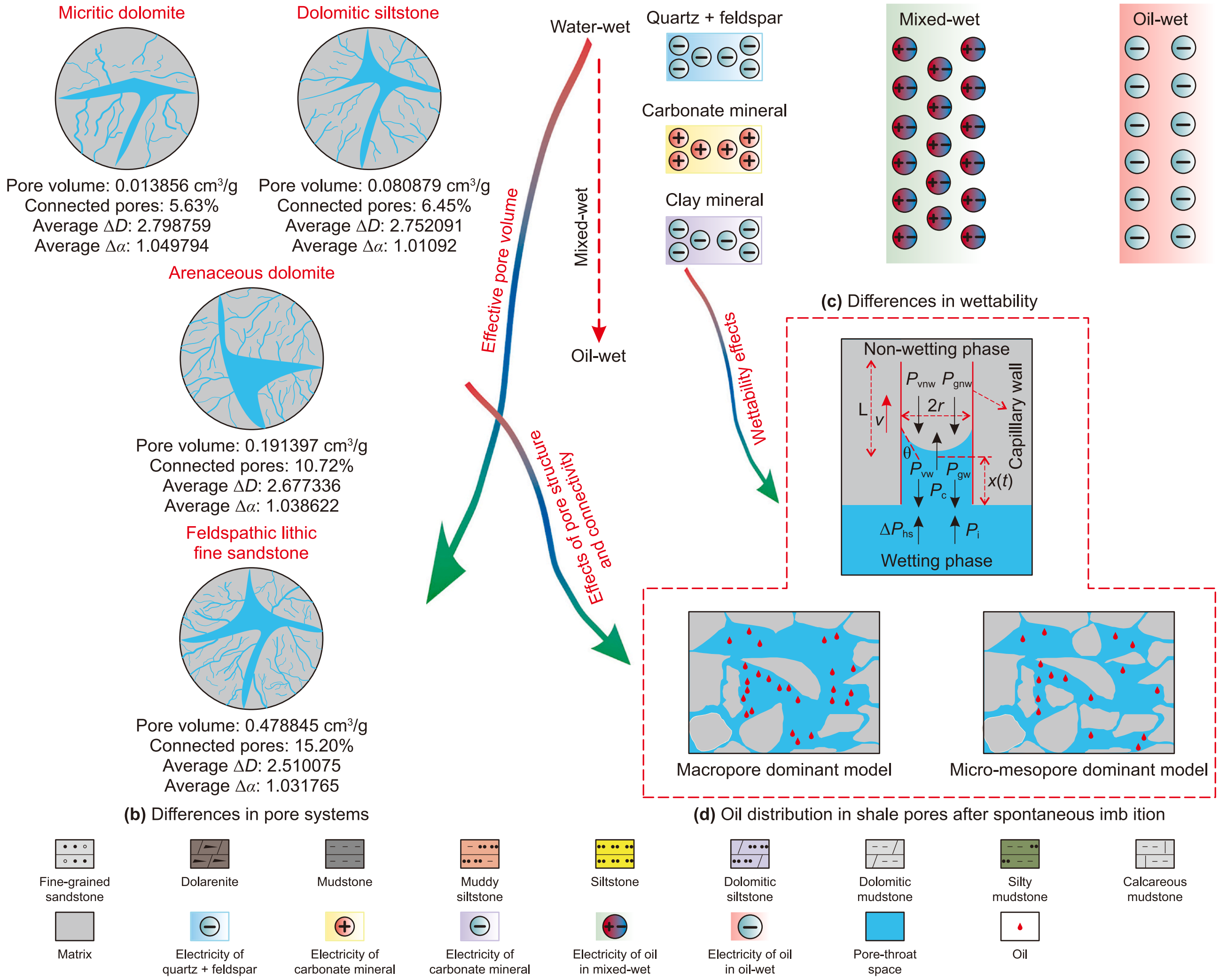

(b) Differences in pore systems

(c) Differences in wettability

(d) Oil distribution in shale pores after spontaneous imb ition

Fig. 15. Flow mechanism of shale oil during pressurized spontaneous imbibition in the Lucaogou Formation, Jimusar Sag, integrating experimental results from Well J10060 (depth >4200 m) and regional stratigraphic framework (Well J174, depth <3400 m) (modified from Tian et al., 2021). P_c is the capillary pressure, ΔP_{hs} is a hydrostatic pressure difference, P_i is the inertial force, P_v is the viscous force, P_g is the gravity, *L* is the capillary length, *r* is the radius of the capillary or rock pore, *x* is the imbibition distance, *t* is the imbibition time, *θ* is a three-phase contact angle, and *v* is the imbibition rate. Besides, the wetting phase and non-wetting phase are represented by subscripts w and nw, respectively.

pressure conditions, fracture matrix coupling structures accelerate imbibition and enhance recovery (Guo et al., 2021). CO_2 flooding experiments further indicate that moderate formation stress can optimize pore-fracture networks, achieving oil recovery up to ten times that of water flooding at 25 MPa (Zhang et al., 2022), highlighting the critical role of pressure and temperature in governing fluid transport mechanisms. Although this study attempts to simulate the reservoir conditions of the Lucaogou Formation at 75 °C and 27 MPa, limitations remain in fully replicating in-situ conditions, and the use of a single sample fails to capture the strong heterogeneity of shale. To improve the reliability and generalizability of the conclusions, future research should implement systematic sampling strategies by collecting multiple core samples from various depth intervals in adjacent wells. On this basis, increasing the number of experiments across a wider range of lithologies and reservoir conditions is essential to comprehensively evaluate the impact of reservoir heterogeneity on imbibition behavior.

5. Conclusions

This study systematically elucidates the multidimensional control mechanisms of pore parameters and wettability on shale oil recovery during pressurized spontaneous imbibition in the Lucaogou Formation. Key findings are as follows.

(1) Shale samples of different lithologies exhibit significant variations in pore size, heterogeneity, and connectivity. Feldspathic lithic fine sandstone and dolomitic siltstone possess higher pore connectivity and lower heterogeneity, indicating superior reservoir quality, while micritic dolomite displays the most complex pore structure and the poorest connectivity, resulting in the weakest reservoir performance. Pore connectivity shows a very strong positive correlation with oil recovery, and the volumes of mesopores and microfractures contribute significantly to recovery. Additionally, the parameters $\Delta\alpha$ and ΔD reflect the structural complexity of the pore network; although they do not directly enhance recovery, their increase can indirectly regulate displacement efficiency during the later stages of imbibition by influencing flow pathways and connectivity.

(2) The wettability characteristics of pores at different scales in the Lucaogou shale vary significantly. Micropore wettability is primarily governed by the surface chemistry of minerals, where oil-wet minerals enhance oil affinity through preferential adsorption, but its correlation with recovery is weak. Mesopore wettability is strongly influenced by the pore network structure and shows a moderate positive correlation with recovery. Macropore wettability is mainly controlled by capillary forces; although the correlation is relatively low, weakly oil-wet to mixed-wet conditions facilitate the formation of continuous oil pathways and enhance displacement efficiency.

(3) Based on the interplay of mineral composition, pore structure, wettability, and capillary forces in shale reservoirs, two distinct residual oil distribution models and their controlling mechanisms were identified: (a) The micropore-mesopore-dominated residual oil retention model occurs primarily in oil-wet lithologies such as micritic dolomites, where low pore connectivity and high capillary resistance result in low displacement efficiency. (b) The macropore-dominated residual oil aggregation model is observed in feldspathic lithic fine sandstone and certain transitional lithologies, where enhanced water-wet and high pore connectivity significantly improve displacement efficiency by promoting oil droplet aggregation.

CRediT authorship contribution statement

Xiao-Biao He: Writing – review & editing, Writing – original draft, Resources, Project administration. **Qun Luo:** Writing – review & editing, Writing – original draft. **Zhen-Xue Jiang:** Resources, Project administration. **Qing-Qing Fan:** Writing – original draft. **Ying-Yan Li:** Formal analysis, Data curation.

Data availability

Data will be made available on request.

Declaration of competing interest

The authors declare that they have no known competing financial interests or personal relationships that could have appeared to influence the work reported in this paper.

Acknowledgement

This work is financially supported by National Natural Science Foundation of China (4167020295) and the Strategic Cooperation Technology Project of CNPC and CUPB (ZLZX 2020-01-05).

References

Afari, S.A., Ling, K.G., Maxey, D., Sennaoui, B., Porlles, J.H., 2023. Experimental investigation of gaseous solvent huff-n-puff in the middle bakken formation. Pet. Sci. 20, 3488–3497. https://doi.org/10.1016/j.petsci.2023.07.007.

Al-Garadi, K., El-Husseiny, A., Elsayed, M., Connolly, P., Mahmoud, M., Johns, M., Adebayo, A., 2022. A rock core wettability index using NMR T_2 measurements. J. Petrol. Sci. Eng. 208, 109386. https://doi.org/10.1016/j.petrol.2021.109386.

Altawati, F., Emadi, H., Pathak, S., 2021. Improving oil recovery of eagle ford shale samples using cryogenic and cyclic gas injection methods-an experimental study. Fuel 302, 121170. https://doi.org/10.1016/j.fuel.2021.121170.

Cai, J., Jiao, X., Wang, H., He, W., Xia, Y., 2024. Multiphase fluid-rock interactions and flow behaviors in shale nanopores: A comprehensive review. Earth Sci. Rev. 257, 104884. https://doi.org/10.1016/j.earscirev.2024.104884.

Cai, J., Qin, X., Wang, H., Xia, Y., Zou, S., 2025. Pore-scale investigation of forced imbibition in porous rocks through interface curvature and pore topology analysis. J. Rock Mech. Geotech. Eng. 17, 245–257. https://doi.org/10.1016/j.jrmge.2024.02.047.

Cao, X., Li, Q., Myers, M., Xu, L., Chen, Q., Tan, Y., 2023. Nanofluid impact on fluid interaction and migration characteristics for enhanced oil recovery in Baikouquan tight glutenite. Advances in Geo-Energy Research 9 (2), 94–105. https://doi.org/10.46690/ager.2023.08.03.

Cao, Y., Jin, Z., Zhu, R., Liu, K., Liu, K., 2024a. Pore systems and their correlation with oil enrichment in various lithofacies of saline lacustrine shale strata. Int. J. Coal Geol. 282, 104444. https://doi.org/10.1016/j.coal.2024.104444.

Cao, Y., Jin, Z., Zhu, R., Liu, K., Bai, J., 2024b. Comprehensive evaluation of the organic-rich saline lacustrine shale in the Lucaogou Formation, Jimusar Sag, Junggar Basin, NW China. Energy 294, 130786. https://doi.org/10.1016/j.energy.2024.130786.

Chen, S., Wang, H., Li, F., Li, P., Zhou, T., Li, N., Xu, L., Zhang, J., 2025. Classification systems of pore-fractures structures and its effects on fracturing fractures propagation in shale reservoir. Geoenergy Sci. Eng. 244, 213409. https://doi.org/10.1016/j.geoen.2024.213409.

Cui, R., Hassanizadeh, S.M., Sun, S., 2022. Pore-network modeling of flow in shale nanopores: Network structure, flow principles, and computational algorithms. Earth Sci. Rev. 234, 104203. https://doi.org/10.1016/j.earscirev.2022.104203.

Du, M., Yang, Z., Jiang, E., Lv, J., Yang, T., Wang, W., Wang, J., Zhang, Y., Li, H., Xu, Y., 2024a. Using digital cores and nuclear magnetic resonance to study pore-fracture structure and fluid mobility in tight volcanic rock reservoirs. J. Asian Earth Sci. 259, 105890. https://doi.org/10.1016/j.jseaes.2023.105890.

Du, M., Zhengming, Y., Lv, W., Xiao, Q., Xiang, Q., Yao, L., Feng, C., 2024b. Experimental study on microscopic production characteristics and influencing factors during dynamic imbibition of shale reservoir with online NMR and fractal theory. Energy 310, 133244. https://doi.org/10.1016/j.energy.2024.133244.

Elkhatib, O., Tetteh, J., Ali, R., Mohamed, A.I.A., Bai, S., Kubelka, J., Piri, M., Goual, L., 2024. Wettability of rock minerals and the underlying surface forces: a review of the implications for oil recovery and geological storage of CO_2. Adv. Colloid Interface Sci. 333, 103283. https://doi.org/10.1016/j.cis.2024.103283.

Emmings, J., Dowey, P., Taylor, K., Davies, S., Vane, C., 2020. Origin and implications of early diagenetic quartz in the Mississippian Bowland Shale Formation, Craven Basin, UK. Marine and Petroleum Geology 120, 104567. https://doi.org/10.1016/j.marpetgeo.2020.104567.

Fan, Y., Liu, K., Yu, L., Liu, J., 2022. Assessment of multi-scale pore structures and pore connectivity domains of marine shales by fractal dimensions and correlation lengths. Fuel 330, 125463. https://doi.org/10.1016/j.fuel.2022.125463.

Fleury, M., Deflandre, F., 2003. Quantitative evaluation of porous media wettability using NMR relaxometry. Magn. Reson. Imaging 21, 385–387. https://doi.org/10.1016/S0730-725X(03)00145-0.

French, K.L., Birdwell, J.E., Lewan, M.D., 2020. Trends in thermal maturity indicators for the organic sulfur-rich Eagle Ford Shale. Mar. Petrol. Geol. 118, 104459. https://doi.org/10.1016/j.marpetgeo.2020.104459.

Fu, C., Kou, X., Du, Y., Jiang, L., Sang, S., Pan, Z., 2025. Experimental study of supercritical CO_2-H_2O-coal interactions and the effect on coal spontaneous imbibition characteristics. Fuel 383, 133888. https://doi.org/10.1016/j.fuel.2024.133888.

Gao, Z., Bai, L., Hu, Q., Yang, Z., Jiang, Z., Wang, Z., Xin, H., Zhang, L., Yang, A., Jia, L., Liu, Z., Ma, G., 2024. Shale oil migration across multiple scales: A review of characterization methods and different patterns. Earth Sci. Rev. 254, 104819. https://doi.org/10.1016/j.earscirev.2024.104819.

Gouyet, J.-F., Bug, A.L.R., 1997. Physics and fractal structures. Am. J. Phys. 65, 676–677. https://doi.org/10.1119/1.18629.

Guo, Q., Xu, S., Hao, F., Yang, F., Zhang, B., Shu, Z., Zhang, A., 2019. Full-scale pores and micro-fractures characterization using FE-SEM, gas adsorption, nano-CT and micro-CT: A case study of the Silurian Longmaxi Formation shale in the Fuling area, Sichuan Basin, China. Fuel 253, 167–179. https://doi.org/10.1016/j.fuel.2019.04.116.

Guo, X., Semnani, Amir, Destina, Godwin, Gao, Z., 2021. Experimental study of spontaneous imbibition for oil recovery in tight sandstone cores under high pressure high temperature with low field nuclear magnetic resonance. J. Petrol. Sci. Eng. 201, 108366. https://doi.org/10.1016/j.petrol.2021.108366.

Guo, Z., Zhao, W., Liu, W., Jiang, H., Gu, Z., Xie, Z., 2025. A comprehensive review of the characteristics, formation, evolution, resource potential, and ultradeep exploration fields of oil-cracking gas in the Ediacaran–Cambrian formations of the Sichuan super gas basin. Mar. Petrol. Geol. 173, 107271. https://doi.org/10.1016/j.marpetgeo.2024.107271.

Han, Y., Jiang, Z., Liang, Z., Lai, Z., Wu, Y., Shi, X., Duan, X., Zhang, Y., Li, Y., 2024. Study on the multifractal characterization and seepage of the shale matrix: A case study of the Longmaxi Formation in Southwestern Sichuan Basin, China. Geoenergy Sci. Eng. 238, 212924. https://doi.org/10.1016/j.geoen.2024.212924.

Hosseini, M., Arif, M., Keshavarz, A., Iglauer, S., 2021. Neutron scattering: A subsurface application review. Earth Sci. Rev. 221, 103755. https://doi.org/10.1016/j.earscirev.2021.103755.

Hosseini, M., Javaherian, A., Movahed, B., 2014. Determination of permeability index using stoneley slowness analysis, NMR models, and formation evaluations: A case study from a gas reservoir, south of Iran. J. Appl. Geophys. 109, 80–87. https://doi.org/10.1016/j.jappgeo.2014.07.016.

Hu, J., Yang, S., Wang, B., Deng, H., Wang, M., Li, J., Zhao, S., Shen, B., Gao, X., Yang, K., 2024. Effect of pore structure characteristics on gas-water seepage behaviour in deep carbonate gas reservoirs. Geoenergy Sci. Eng. 238, 212881. https://doi.org/10.1016/j.geoen.2024.212881.

Jia, H., Zhang, R., Luo, X., Zhou, Z., Yang, L., 2024. Nuclear magnetic resonance experiments on the time-varying law of oil viscosity and wettability in high-multiple waterflooding sandstone cores. Petrol. Explor. Dev. 51, 394–402. https://doi.org/10.1016/S1876-3804(24)60031-5.

Jin, Z., Zhu, R., Liang, X., Shen, Y., 2021. Several issues worthy of attention in current lacustrine shale oil exploration and development. Petrol. Explor. Dev. 48, 1471–1484. https://doi.org/10.1016/S1876-3804(21)60303-8.

Kong, D., Peng, Y., Zhou, Z., Peng, H., Chen, Z., 2024. Pore-scale mechanism of coupled pressure-driven flow and spontaneous imbibition in porous media during high-pressure water injection processes. Capillarity 13 (2), 29–36. https://doi.org/10.46690/capi.2024.11.01.

Li, K., Xi, K., Cao, Y., Shan, X., Lin, M., 2024. Diagenetic alterations induced by lamina-scale mass transfer and the impacts on shale oil reservoir formation in carbonate-rich shale of the Permian Lucaogou Formation, Jimusar Sag. Mar. Petrol. Geol. 162, 106709. https://doi.org/10.1016/j.marpetgeo.2024.106709.

Lin, Z., Hu, Q., Yin, N., Yang, S., Liu, H., Chao, J., 2024. Nanopores-to-microfractures flow mechanism and remaining distribution of shale oil during dynamic water dynamic imbibition studied by NMR. Geoenergy Sci. Eng. 241, 213202. https://doi.org/10.1016/j.geoen.2024.213202.

Liu, Q., Li, J., Liang, B., Liu, J., Sun, W., He, J., Lei, Y., 2023. Complex wettability behavior triggering mechanism on imbibition: A model construction and comparative study based on analysis at multiple scales. Energy 275, 127434. https://doi.org/10.1016/j.energy.2023.127434.

Looyestijn, Wim, Jan Hofman, 2006. Wettability-index determination by nuclear magnetic resonance. SPE Reservoir Eval. Eng. 9, 146–153. https://doi.org/10.2118/93624-PA.

Luo, Q., Gong, L., Qu, Y., Zhang, K., Zhang, G., Wang, S., 2018. The tight oil potential of the Lucaogou Formation from the southern Junggar Basin, China. Fuel 234, 858–871. https://doi.org/10.1016/j.fuel.2018.07.002.

Lv, Q., Hou, J., Chen, J., Ji, Y., Cheng, Z., Lv, J., Zhong, J., 2025. Experimental study on elastic development characteristics and imbibition mechanism of shale oil reservoirs at micro-nano scale. Fuel 381, 133557. https://doi.org/10.1016/j.fuel.2024.133557.

Pang, X., Li, M., Li, B., Wang, T., Hui, S., Liu, Y., Liu, G., Hu, T., Xu, T., Jiang, F., Pang, H., Wang, C., 2023. Main controlling factors and movability evaluation of continental shale oil. Earth Sci. Rev. 243, 104472. https://doi.org/10.1016/j.earscirev.2023.104472.

Sharifigaliuk, H., Mahmood, S.M., Rezaee, R., Saeedi, A., 2021. Conventional methods for wettability determination of shales: A comprehensive review of challenges, lessons learned, and way forward. Mar. Petrol. Geol. 133, 105288. https://doi.org/10.1016/j.marpetgeo.2021.105288.

Sun, S., Zhang, B., Wang, X., Xiao, W., Tian, H., Hou, G., Zhang, S., 2024. High-resolution geochemistry in the Lucaogou Formation, Junggar Basin: Climate fluctuation and organic matter enrichment. Mar. Petrol. Geol. 162, 106734. https://doi.org/10.1016/j.marpetgeo.2024.106734.

Tangparitkul, S., Sukee, A., Jiang, J., Tapanya, C., Fongkham, N., Yang, H., 2023. Role of interfacial tension on wettability-controlled fluid displacement in porous rock: a capillary-dominated flow and how to control it. Capillarity 9 (3), 55–64. https://doi.org/10.46690/capi.2023.12.02.

Tian, W., Wu, K., Gao, Y., Chen, Z., Gao, Y., Li, J., 2021. A critical review of enhanced oil recovery by imbibition: theory and practice. Energy Fuels 35, 5643–5670. https://doi.org/10.1021/acs.energyfuels.1c00199.

Turcotte, D.L., 2002. Fractals in petrology. Lithos 65, 261–271. https://doi.org/10.1016/S0024-4937(02)00194-9.

Wang, B., Cao, R., Pi, Z., Cheng, L., Jia, Z., Hu, J., 2024. Displacement-imbibition coupling mechanisms between matrix and complex fracture during injecting-shut in-production process using pore-scale simulation and NMR experiment. Geoenergy Sci. Eng. 242, 213254. https://doi.org/10.1016/j.geoen.2024.213254.

Wang, J.J., Zhang, P.F., Lu, S.F., Lin, Z.Z., Li, W.B., Zhang, J.J., Gao, W.Z., Zhou, N.W., Chen, G.H., Yin, Y.J., Wu, H., 2025. Insights into microscopic oil occurrence characteristics in shales from the Paleogene funing formation in Subei Basin, China. Pet. Sci. 22, 55–75. https://doi.org/10.1016/j.petsci.2024.07.025.

Wang, L., Tian, Y., Yu, X., Wang, C., Yao, B., Wang, S., Winterfeld, P.H., Wang, X., Yang, Z., Wang, Y., Cui, J., Wu, Y.-S., 2017. Advances in improved/enhanced oil recovery technologies for tight and shale reservoirs. Fuel 210, 425–445. https://doi.org/10.1016/j.fuel.2017.08.095.

Wang, Y., Cao, J., Tao, K., Li, E., Ma, C., Shi, C., 2020. Reevaluating the source and accumulation of tight oil in the middle Permian Lucaogou Formation of the Junggar Basin, China. Mar. Petrol. Geol. 117, 104384. https://doi.org/10.1016/j.marpetgeo.2020.104384.

Wijaya, N., Sheng, J., 2022. Effect of compaction and imbibition on benefits of drawdown management in shale oil production: Uncertainty in recovery driving mechanisms. J. Petrol. Sci. Eng. 210, 110014. https://doi.org/10.1016/j.petrol.2021.110014.

Xiao, D., Zheng, L., Wang, M., Wang, R., Guan, X., 2024. The relationship between oiliness and mobility and their controlling factors for lacustrine shale oil: A case study of Qing1 member in Changling Sag, Songliao Basin. Fuel 376, 132738. https://doi.org/10.1016/j.fuel.2024.132738.

Xia, Y., Tian, Z., Xu, S., Wei, W., Cai, J., 2021. Effects of microstructural and petrophysical properties on spontaneous imbibition in tight sandstone reservoirs. Journal of Natural Gas Science and Engineering 96, 104225. https://doi.org/10.1016/j.jngse.2021.104225.

Xiao, Y., You, Z., He, Y., Du, Z., Zheng, J., Wang, L., 2025. Capillary-dominated imbibition in heterogeneous-wet reservoirs: Mechanisms, characterizations, and critical insights. Geoenergy Sci. Eng. 246, 213606. https://doi.org/10.1016/j.geoen.2024.213606.

Yan, X., Dai, C., Wang, R., Liu, H., Meng, S., Jin, X., Hu, Y., Wu, Y., 2024. Experimental study on countercurrent imbibition in tight oil reservoirs using nuclear magnetic resonance and AFM: Influence of liquid-liquid/solid interface characteristics. Fuel 358, 130026. https://doi.org/10.1016/j.fuel.2023.130026.

Yang, W., Yang, R., Wang, M., Bao, S., Yang, L., Hou, H., 2025. Impact of lithofacies categories on inflection-point behaviors in micro-nano pore-structure evolution: implications for differential reservoir-forming mechanisms and "sweet-spot intervals" identification for marine gas shales. Mar. Petrol. Geol. 176, 107336. https://doi.org/10.1016/j.marpetgeo.2025.107336.

Yuan, M., Zou, C., Pan, S., Zhang, G., Shi, Q., Xie, L., Zhao, Z., Shen, Y., Jing, Z., 2024. Ranking the oil contribution of individual layers in a lacustrine shale oil system based on non-hydrocarbon analysis by FT-ICR MS. Int. J. Coal Geol. 288, 104528. https://doi.org/10.1016/j.coal.2024.104528.

Zhang, Q., Liu, Y., Wang, B., Ruan, J., Yan, N., Chen, H., Wang, Q., Jia, G., Wang, R., Liu, H., Xue, C., Liu, F., Yang, H., Zhu, Y., 2022. Effects of pore-throat structures on the fluid mobility in chang 7 tight sandstone reservoirs of longdong area, Ordos Basin. Mar. Petrol. Geol. 135, 105407. https://doi.org/10.1016/j.marpetgeo.2021.105407.

Zhang, T., Hu, Q., Xiao, Y., Nagy, G., Yang, S., Yuan, B., Jiang, H., 2024a. Wetting mechanism and alteration of nano-sized shale pores: Insights from contrast variation small angle neutron scattering. J. Mol. Liq. 413, 125962. https://doi.org/10.1016/j.molliq.2024.125962.

Zhang, Z., Zhang, T., Liu, H., Li, X., Xu, D., 2024b. Control and prediction of bedding-parallel fractures in fine-grained sedimentary rocks: A case from the Permian

Lucaogou Formation in Jimusar Sag, Junggar Basin, Western China. Pet. Sci. 21, 3815–3838. https://doi.org/10.1016/j.petsci.2024.09.003.

Zheng, H., Yang, F., Guo, Q., Liu, K., 2025. Upscaling characterizing pore connectivity, morphology and orientation of shale from nano-scale to micro-scale. Mar. Petrol. Geol. 172, 107213. https://doi.org/10.1016/j.marpetgeo.2024.107213.

Zheng, S., Yao, Y., Liu, D., Cai, Y., Liu, Y., Li, X., 2019. Nuclear magnetic resonance T_2 cutoffs of coals: A novel method by multifractal analysis theory. Fuel 241, 715–724. https://doi.org/10.1016/j.fuel.2018.12.044.

Zhu, H., Huang, C., Ju, Y., Bu, H., Li, X., Yang, M., Chu, Q., Feng, H., Qiao, P., Qi, Y., Ma, P., Zheng, L., Lu, Y., 2021. Multi-scale multi-dimensional characterization of clay-hosted pore networks of shale using FIB-SEM, TEM, and X-ray micro-tomography: implications for methane storage and migration. Appl. Clay Sci. 213, 106239. https://doi.org/10.1016/j.clay.2021.106239.

Zou, C., Zhao, Q., Zhang, G., Xiong, B., 2016. Energy revolution: from a fossil energy era to a new energy era. Nat. Gas. Ind. B 3, 1–11. https://doi.org/10.1016/j.ngib.2016.02.001.